

## Mémoire

**Auteur** : Lalou, Quentin

**Promoteur(s)** : 8567; Rauw, Grégor

**Faculté** : Faculté des Sciences

**Diplôme** : Master en sciences spatiales, à finalité approfondie

**Année académique** : 2022-2023

**URI/URL** : <http://hdl.handle.net/2268.2/18845>

---

### *Avertissement à l'attention des usagers :*

*Tous les documents placés en accès ouvert sur le site le site MatheO sont protégés par le droit d'auteur. Conformément aux principes énoncés par la "Budapest Open Access Initiative"(BOAI, 2002), l'utilisateur du site peut lire, télécharger, copier, transmettre, imprimer, chercher ou faire un lien vers le texte intégral de ces documents, les disséquer pour les indexer, s'en servir de données pour un logiciel, ou s'en servir à toute autre fin légale (ou prévue par la réglementation relative au droit d'auteur). Toute utilisation du document à des fins commerciales est strictement interdite.*

*Par ailleurs, l'utilisateur s'engage à respecter les droits moraux de l'auteur, principalement le droit à l'intégrité de l'oeuvre et le droit de paternité et ce dans toute utilisation que l'utilisateur entreprend. Ainsi, à titre d'exemple, lorsqu'il reproduira un document par extrait ou dans son intégralité, l'utilisateur citera de manière complète les sources telles que mentionnées ci-dessus. Toute utilisation non explicitement autorisée ci-avant (telle que par exemple, la modification du document ou son résumé) nécessite l'autorisation préalable et expresse des auteurs ou de leurs ayants droit.*

---



Royal Observatory  
of Belgium

*Master's Thesis*

---

**Study and modeling of the bouncing motion of Juventas on  
Dimorphos**

---

Author: Quentin Lalou  
Academic Year 2022-2023  
Department of astrophysics geology and oceanography  
Master in Space Sciences - Academic Focus  
Supervisor: Özgür Karatekin  
Co-Supervisor: Gregor Rauw  
Readers : Bart Van Hove, Onur Çelik, Denis Grodent

## Abstract

The AIDA collaboration between the NASA and the ESA aims to deviate the binary asteroid system Didymos. At the date of this thesis, the DART mission has already occurred. Its objective was to impact the asteroid Dimorphos to deviate it. Considering the recent measurements, it is a success. In particular, the HERA mission, developed by ESA, will study the asteroid Dimorphos, which is part of a binary system conjointly with a bigger asteroid Didymos. The spacecraft will carry 2 cubesats that will land on the surface of Dimorphos, and will eventually bounce on its surface. In this context, this thesis has as objective to simulate the bounce of Juventas on the surface of Dimorphos and study it through a Monte-Carlo analysis. By varying the surface properties, the position and speed of the spacecraft, we aim to collect some information about the success of the mission. A new algorithm has been developed accounting for the rotation of the spacecraft and its 3D shape. The result of this new model will be studied. Results have shown dependencies between the coefficient of restitutions, incident angle and contact time. According to the new mission, the mission should not fail and Juventas will not bounce off of Dimorphos. Another study will be made with a noise that will be applied on the surface of the asteroid to see the impact of small deformations on the bounce of the spacecraft, showing an increase of the dispersion with an increasing noise.

## Acknowledgement

I would like to thank Özgür Karatekin from the Royal Observatory of Belgium for giving me the opportunity to work on this subject that I found infinitely interesting. His help for this thesis was always welcome, and he made a fantastic mentor. Also from ROB, I have to thank Guillaume Noiset, who helped throughout this entire endeavor. He supervised my progress, reviewed my thesis, provided me with various advice, and guided my work. He answered each of my questions with great patience, and I'm truly grateful to him for that.

A huge thanks to Guillaume Vanhalst, Guillaume Hanon and Guillaume Roisin for the previous studies they have done. Their code allowed to build this study and I hope I could continue to extend their work.

I would also like to say a huge thank you to Gregor Rauw, who accepted to be my co-promotor during the year. He was also very patient and followed the progress of my work, and helped me with precious advices.

My readers also deserve a huge thank you. Onur Çelik, Bart Van Hove and Denis Grodent, for accepting to be my readers and to review my work.

During the thesis, I was helped by the employees of GMV, Victor Manuel Moreno Villa and Adalberto Dominguez Castillo who gave me important data on the Juventas mission. From Gomspace, Mehdi Coubeau gave me also a lot of information on the design of the CubeSat.

Finally, I would like to thank Vasco Lenzi, who helped me to understand the physics engine used in the thesis.

# Contents

<b>1</b>	<b>Mission description</b>	<b>7</b>
1.1	AIDA . . . . .	7
1.1.1	DART . . . . .	7
1.1.2	Hera . . . . .	8
1.2	Didymos system . . . . .	9
1.3	Juventas . . . . .	11
1.3.1	Science objectives & mission profile . . . . .	11
<b>2</b>	<b>Dynamic modeling</b>	<b>16</b>
2.1	Circular Restricted 3-Body Problem . . . . .	16
2.2	Gravity perturbation . . . . .	17
2.2.1	Gravity of Didymos . . . . .	17
2.2.2	Gravity of Dimorphos . . . . .	18
2.3	Perturbed Circular-Restricted 3 body problem . . . . .	19
2.4	Solar radiation pressure . . . . .	20
2.5	Braking maneuver . . . . .	20
<b>3</b>	<b>Modeling of Bouncing Motion</b>	<b>22</b>
3.1	Surface collision . . . . .	22
3.2	Point-Like Bouncing Model . . . . .	24
3.3	3D Bouncing Model . . . . .	25
3.3.1	Physics engine . . . . .	25
3.3.2	Contact Force . . . . .	26
3.3.3	Geometry . . . . .	29
3.3.4	Hinges . . . . .	30
3.3.5	Stop condition . . . . .	31
3.3.6	Overall implementation . . . . .	32
3.3.7	Physics Engine Solver . . . . .	33
3.3.8	Free rotation . . . . .	33
<b>4</b>	<b>Numerical Method</b>	<b>34</b>
4.1	Runge-Kutta Fehlberg . . . . .	34
4.2	Time step reduction on the surface . . . . .	35
4.3	Vectorization . . . . .	36
4.4	Implementation of the bouncing motion . . . . .	36
4.5	Validation . . . . .	37
<b>5</b>	<b>Surface deformation</b>	<b>40</b>
5.1	Rocks population . . . . .	40
5.1.1	Rocks placement . . . . .	41
5.1.2	Rock's shapes definition . . . . .	42
5.1.3	Fit to the surface . . . . .	43

5.1.4	Parameters of rocks . . . . .	45
5.2	Shape Model Deformation . . . . .	46
5.2.1	Perlin Noise . . . . .	46
5.2.2	Mapping . . . . .	47
5.2.3	Resolution . . . . .	48
<b>6</b>	<b>Monte-Carlo Analysis</b>	<b>50</b>
6.1	Preliminaries . . . . .	50
6.1.1	Uncertainties . . . . .	50
6.1.2	Convergence . . . . .	51
6.2	Landing and bouncing trajectories . . . . .	54
6.3	Coefficient of restitution . . . . .	56
6.4	Solar panels . . . . .	64
6.5	Retraction of solar panels . . . . .	67
<b>7</b>	<b>Surface variation</b>	<b>69</b>
7.1	Perlin noise . . . . .	69
7.2	Rock population . . . . .	69
<b>8</b>	<b>Conclusions</b>	<b>73</b>
8.1	Improvements of the model . . . . .	73
8.2	Implication for the mission . . . . .	74
8.3	Terrain roughness . . . . .	74
8.4	Suggestions for Future Work . . . . .	75

## Introduction

During the Rosetta mission, the Philae was supposed to land on the site J (named later Agilkia) of the comet 67P/Tchourioumov-Guérassimenko. It was equipped with an anchor system and thruster to stick on the ground when the first contact with the surface. Unfortunately, a critical failure on those systems led the spacecraft to bounce instead of landing. Due to the weak gravity force, the lander bounced during nearly 2 hours, before coming at rest in an unsecure position, with a lower illumination than expected perturbing the thermal control of the probe and the power production of solar panels. Even if the probe could make some measurements, the operators went through a lot of trouble to solve the problems caused by this uncontrolled landing and the measurements could be done mainly by luck. The study of bounces seems to be a field of interest for future missions which aim to land on small, airless bodies of the solar system. In this context, this work aims to provide a new model to describe the bounces of the Juventas spacecraft on an asteroid during the Hera mission, with an emphasis on the 3D shape of it and its rotations.

Before introducing the Hera mission, a presentation about its predecessor, DART, must be provided. The Double Asteroid Redirection Test (DART) mission, spearheaded by NASA, launched in 2021 aimed to modify the velocity of Dimorphos, an asteroid from the binary system Didymos, through an impact. In September 26 2022, the DART successfully hit its target and deflected the asteroid. The impact was even more effective than expected.

Five years later, it's the Hera mission, led by the European Space Agency, that will reach Dimorphos. It will study the consequences of the previous mission and in particular characterize the crater and the properties of its surface. During the mission, the CubeSat Juventas will be used to scan and land on the surface of the asteroid.

This study is relying on the work of 2 previous theses, the one of Guillaume Hanon and Guillaume Vanhalst "A study of the landing phase of the Juventas CubeSat on the moon of the binary asteroid system Didymos" [43] and the thesis of Guillaume Roidin "Landing trajectories analysis and geophysics of Juventas in the binary asteroid system Didymos" [32] that is an extension of the previous one. During their work, they developed a propagator for the Didymos system that will be used in this thesis, and improved in order to emulate the bounces of the spacecraft.

## Master Thesis Structure

Investigating the trajectories of a spacecraft during bouncing events presents notable challenges due to the inherent complexities associated with both the assumptions made and the nature of the bouncing surface. Frequently, the intricate factors of rotational dynamics and the object's three-dimensional form are overlooked in favor of simplifying the model for efficiency, especially when a big number of trajectories have to be simulated. A precedent has been set by Guillaume Roisin [32], wherein a method embracing these simplifications has been developed. In this context, a new algorithm has been developed, departing from the conventional route

by including the 3D shape and rotational dynamics of the spacecraft. The core of this thesis centers on comprehending the implications of this new model. Also, a method has been set to deform the surface of the asteroid in order to emulate an irregular ground with rocks on its surface. Finally, a Monte-Carlo analysis is performed to study the different parameters of the trajectory.

Chapter 1 introduces the core mission addressed in this thesis and provides essential contextual information. It commences by discussing the AIDA collaboration and its twin missions: DART and Hera. Subsequently, the focus turns towards the Didymos system, elucidating its physical and dynamic characteristics. Finally, the configuration of the Juventas CubeSat, its scientific objectives, and the phases of its mission are outlined.

In Chapter 2 of this thesis, the emphasis is on modeling Juventas' motion within the Didymos system. The chapter commences with the derivation of the equations governing Juventas' motion, taking into account gravitational perturbations and the virtual forces due to the choice of reference frame. Additionally, a discussion ensues on the influence of solar radiation pressure and the braking maneuver.

Chapter 3 delves into the modeling of Juventas' bouncing behavior. It first illustrates collision detection, followed by the physical equations employed to compute the bouncing motion. The geometry of Juventas and its mechanical components are also explored, along with their corresponding modeling techniques. The conditions dictating the cessation of the bouncing behavior are established.

In Chapter 4, the focus shifts to the vectorization method developed by Guillaume Roisin [32], specifically the Runge-Kutta Fehlberg method. The adaptation of this method to incorporate the bouncing behavior is detailed, including the collision detection process for each propagator sample and the overarching algorithmic structure.

Chapter 5 is dedicated to the exploration of surface deformations using two distinct methods. The first method involves the direct placement of generated rocks onto the surface, while the second method involves directly deforming the surface itself through the application of Perlin noise.

Chapter 6 presents the diverse outcomes of the simulations. The establishment of initial conditions is followed by a comprehensive convergence analysis. The results of the simulations are studied, ranging from the landing position of Juventas to the deflection of its solar panels.

In Chapter 7, the focus lies on evaluating the impact of surface deformations on various parameters. Multiple samples are subjected to testing on differing surfaces to discern the influence of noise on the dynamics of bouncing.

The concluding Chapter 8 summarizes the key findings and advancements presented in this thesis, offering insights for potential future endeavors.



# 1 Mission description

This chapter provides contextual information regarding the ongoing mission associated with this thesis. Initially, the AIDA collaboration is introduced, along with its two separate missions : DART and Hera. Subsequently, the Didymos system is presented, including its physical and dynamical parameters. Following that, the Juventas CubeSat is described, outlining its scientific objectives and mission phases. Finally, the landing trajectories are discussed at the end of the chapter.

## 1.1 AIDA

The AIDA (Asteroid Impact Deflection Assessment) collaboration is an international effort involving the NASA and the ESA dedicated to studying and understanding the impact dynamics of asteroids and developing techniques to mitigate potential asteroid threats to Earth. The collaboration aims to improve our understanding of the physics behind asteroid impacts and test the feasibility of asteroid deflection strategies. The designated target for the collaboration is the binary asteroid system 65803 Didymos [24], which consists of a primary asteroid and a smaller moonlet orbiting around it. It was chosen due to the size of the 2 bodies, which are typically the dimension of asteroids that could threaten the Earth. Furthermore, the binary is relatively near to Earth which increases the feasibility of the mission, and the system's disposition allows an easy measurement of the change of speed on the different bodies. The two main missions within the AIDA are DART (Double Asteroid Redirection Test) and Hera. DART, led by NASA, aims to impact the smaller moonlet of Didymos, while Hera, led by the European Space Agency (ESA), will study the impact in detail and provide complementary measurements of the resulting deflection.

### 1.1.1 DART

The DART (Double Asteroid Redirection Test) mission is a project led by NASA with the goal of testing a planetary defense technique for deflecting potential asteroid impacts on Earth, which is the first mission of its kind [23]. DART's target is the asteroid Dimorphos, the moonlet of the Didymos system. A scheme of the mission is shown on the figure 1. .

The objective of DART was to demonstrate the capability of redirecting the trajectory of an asteroid by deliberately crashing into the smaller moonlet. The spacecraft hit its target on September 26 2022 and carried a strong kinetic impact with an impact speed of 6.58 km/s. The deflection was a success, DART induced a modification to the velocity of the celestial body by 2.7 mm/s [3], which was a number beyond the initial expectations.

DART was equipped with advanced technologies, including autonomous navigation and targeting systems, to ensure precise impact on the moonlet. The spacecraft carried carry a 6U CubeSat equipped with an onboard camera system, LICIAcube, developed by the Italian Space Agency and was deployed 15 days prior to impact. Its role was to capture images and data before, during, and after the impact [14]. A picture taken by LICIA is shown on the

figure 2.

Through the DART mission, scientists and engineers aim to improve our understanding of asteroid dynamics, refine impact modeling techniques, and provide crucial data for potential future asteroid deflection missions. By demonstrating the feasibility of kinetic impact as a viable planetary defense method, DART contributes to our ability to protect Earth from potential asteroid threats.

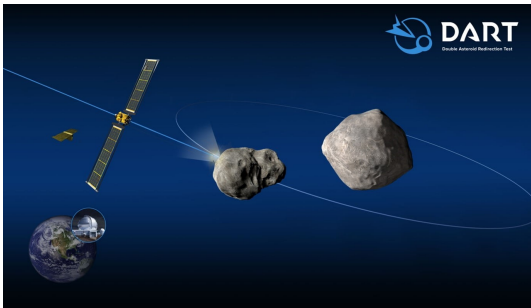


Figure 1: Scheme of the DART mission [23].



Figure 2: Image captured by the LICI-ACube a few minutes after the collision [21].

### 1.1.2 Hera

The Hera mission is a project led by the European Space Agency (ESA) as a part of the AIDA collaboration and scheduled for launch in 2024. Its primary objective is to study and investigate the impact and effects of the Double Asteroid Redirection Test (DART) mission on the binary asteroid system Didymos. It is anticipated to arrive at the Didymos system in 2027, so five years after the impact of DART.

Hera's mission goals encompass a comprehensive analysis of the physical and dynamic properties of the Didymos system following the DART impact. It aims to provide detailed measurements of the deflection caused by DART, along with characterizing the resulting crater and the properties of the ejected material [10]. By doing so, Hera will contribute to our understanding of the effectiveness of the kinetic impact deflection strategy.

The spacecraft will carry a suite of scientific instruments, including asteroid framing cameras, a planetary altimeter, a thermal infrared imager, and two 6U CubeSats named Juventas and Milani [10]. These instruments will enable Hera to collect valuable data on the asteroid's surface, composition, internal structure, and regolith properties. Following approximately two months of observations, Hera will deploy the two CubeSats, each equipped with their own scientific instruments, to gather additional data about the asteroid. Additionally, the mission will focus on studying the moonlet's orbital and rotational dynamics to enhance our under-

standing of binary asteroid systems.

Hera will also serve as a technology demonstrator, testing advanced technologies and systems for future asteroid missions. It will include innovative approaches for small bodies exploration, using real-time navigation system for close operations [37].

The data gathered by Hera will not only contribute to planetary defense strategies but also provide crucial insights into the formation and evolution of asteroids and their role in the early Solar System. By studying the Didymos system up close, Hera will unlock new knowledge and pave the way for future asteroid exploration missions. The overall mission is illustrated on the figure 3.

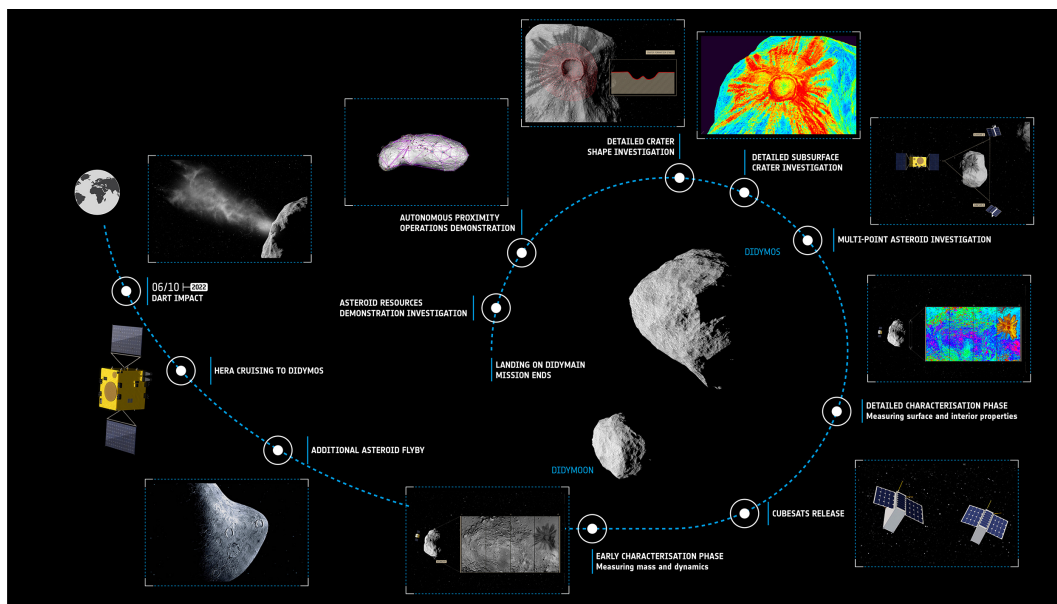


Figure 3: Scheme showing the time line of the Hera mission [9].

## 1.2 Didymos system

The celestial body considered in this thesis is the binary asteroid Didymos, discovered in 1996. Nonetheless, it is only in 2003 that the secondary Dimorphos was discovered. Since it is a Near-Earth Object (NEO), the binary makes an accessible target for the AIDA collaboration, without being too close to the Earth to be an actual threat even after the impact of DART. Furthermore, the Didymos system is ecliptic relative to the Earth, which allows to telescope to perform accurate measurements on the orbital period of Dimorphos thanks to the brightness variations. Furthermore, a main characteristic of the system is the synchronicity between the orbit of Dimorphos and its rotation. Indeed, the period of the orbit is 11h55m, as for the rotation time. Nonetheless, Dimorphos lost this property after the impact of DART [12], but since the thesis focuses more on the development of a tool to explore the bounce of a satellite instead of its accurate propagation, this assumption is made along the thesis to

keep the physical system simpler. It will be a major information during the modeling of the dynamical system. The main parameters of the Didymos system are summarized in the table 1.

The shape of the components of the system is far from spherical. A 3D model of the 2 bodies are shown on figure 4. Furthermore, the recent images of DART 5 suggest a surface with a lot of rocks.

Parameter	Value
Rotation period of the primary	$2.26 \pm 0.0001$ h
Distance between the center of the primary and the secondary	$1.18 +0.004/-0.002$ km
Diameter ratio	$0.21 \pm 0.01$
Orbital period of the secondary	$11.92 +0.004/-0.006$ h
Rotation period of the secondary	$11.93 \pm 0.01$ h [30]
Eccentricity of the orbit of the secondary	$<0.05$ [30]
Diameter of the primary	$0.775 \pm 0.078$ km
Diameter of the secondary	$0.163 \pm 0.018$ km
Total mass of the system	$5.278e11 \pm 0.54e11$ kg
Heliocentric eccentricity	$0.383752501 \pm 7.7e-9$
Heliocentric semi-major axis	$1.6444327821 \pm 9.8e-9$ AU
Heliocentric inclination	$3.4076499 \pm 2.4e-6$ °

Table 1: Table of the different parameters of the Didymos system prior to DART [15].

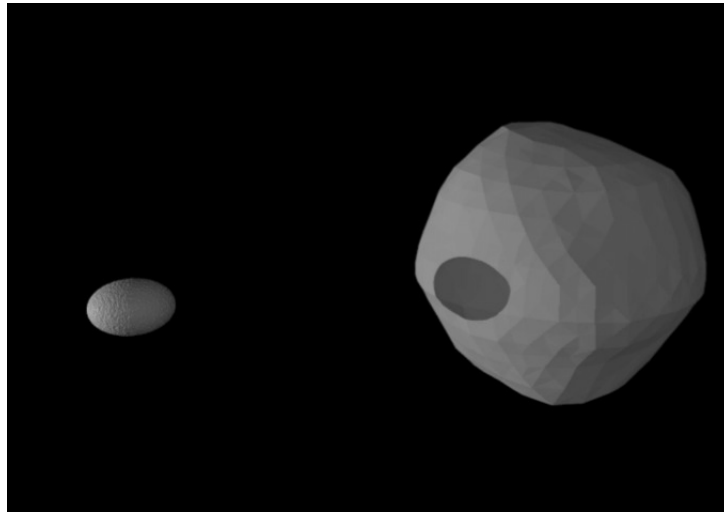


Figure 4: 3D models of Dimorphos and Didymos [22].

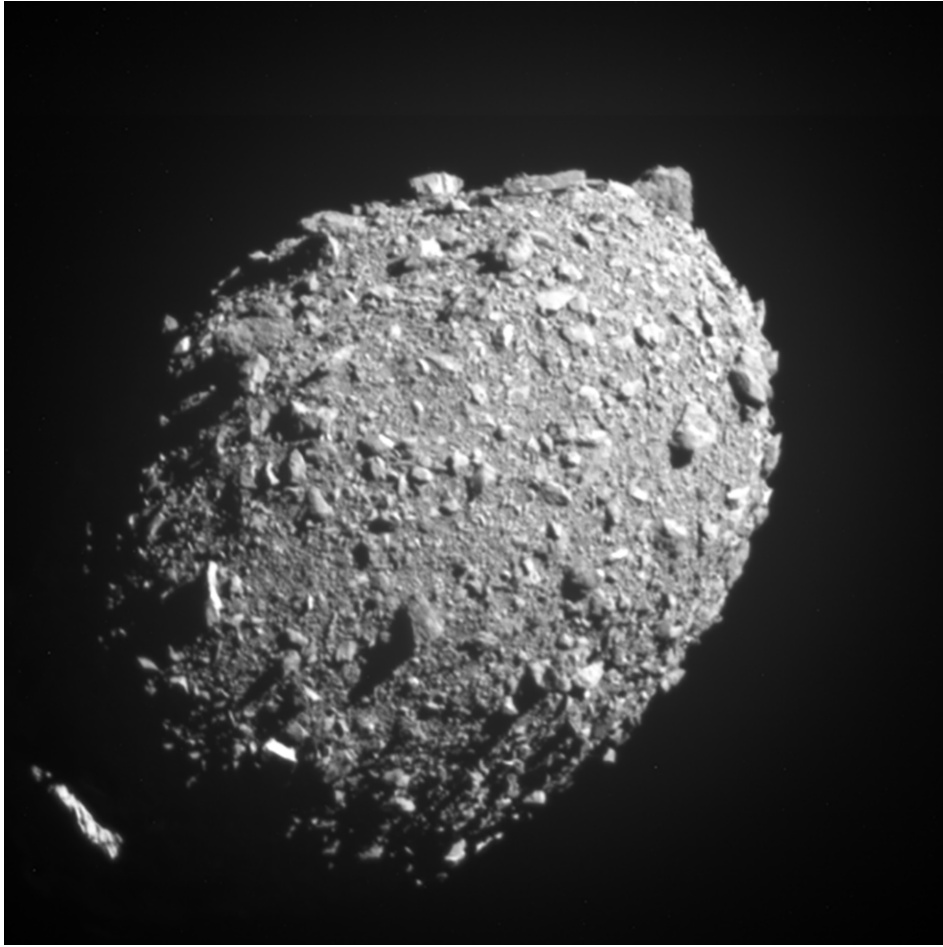


Figure 5: Picture of Dimorphos taken from DART before the impact [13].

### 1.3 Juventas

Juventas is one of the two CubeSats that will be on the Hera spacecraft. With a wet mass of approximately 12 kg [7], the payload is composed of a 3-axis gravimeter, an inertial measurement units (gyroscope + accelerometer), an inter-satellite link, a Low-Frequency Radar and a visible camera, along with the electronics for the Guidance Navigation and Control. The propulsion is assured by a cold-gas propulsion system, and the electric power supply by solar panels and lithium cells batteries. The sun-sensors, star tracker and gyros allow the determination of the attitude of the spacecraft. The CubeSat is equipped with deployable solar panels, that can generate a power up to 35 W at 1.8 AU (astronomical unit). The telecommunications are assured by a 1.36m deployable antenna.

#### 1.3.1 Science objectives & mission profile

Juventas will be focused on the study of Dimorphos and has essentially 4 main objectives :

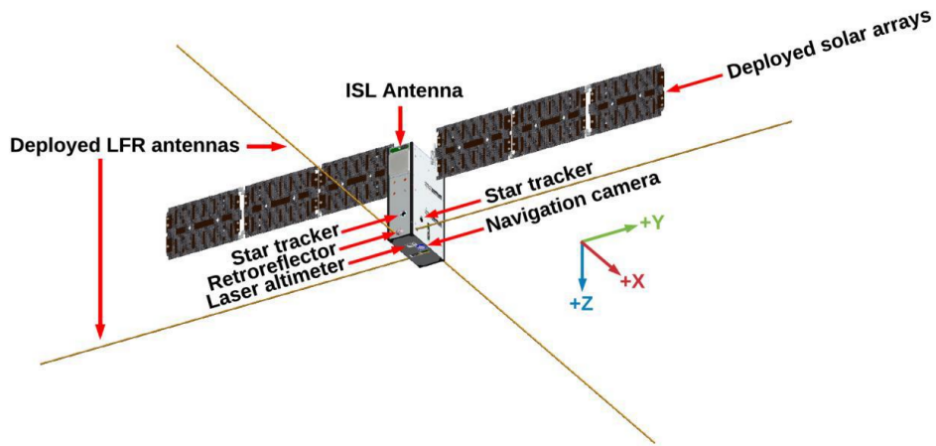


Figure 6: Exterior view of Juventas [35].

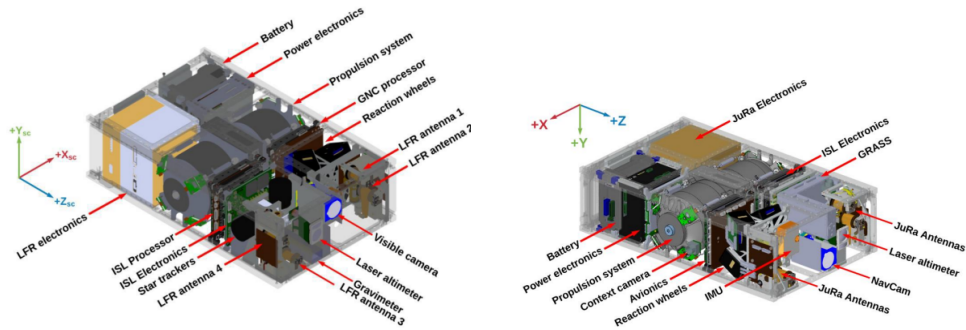


Figure 7: Internal view of Juventas [35].

- Study of the gravity field of Dimorphos
- Study of the internal properties of Dimorphos
- Study of the surface properties of Dimorphos and characterization of the crater of DART
- Study of the dynamical properties of Dimorphos.

The Juventas mission will follow different phases [35]. Here is a summary of each one with a short description, and a time line on the figure 8. The corresponding orbits used for the observations are shown in the figure 9.

**Cubesat Commissioning phase :** During the approach of Hera, right after the release of Juventas, some checks of the systems will be done. This phase will last for 4 days. After that, when Hera will come in the release distance (between 23 and 30km), a low velocity deployment pod will be used to eject the CubeSat.

**Cubesat Insertion Phase (INSP) :** Once all the checkups are done, Juventas is ready for its orbit injection. An hyperbolic trajectory is chosen as such Juventas will perform a maneuver to enter into a Self-Sustainable Terminator Orbit (SSTO) at an altitude of 3.3 km of the Didymos system. The insertion lasts 6 days.

**SSTO 3.3 km :** Once the orbit is stabilized, Juventas will be able to do its first measurements where the surface characterization of the Didymos system will be conducted. The SSTO orbit is nearly perpendicular to the axis between the Sun and the Didymos system. This orbit is selected for its stability and to minimize the required  $\Delta V$  for orbit maintenance along with the sun radiation pressure (SRP). During the observations phases, Juventas remains on the SSTO and carries out its primary objectives using the Low-Frequency Radar (LFR) and radio science measurements with the Inter-Satellite Link (ISL) radio to communicate with the Hera spacecraft. More than 70% coverage of Didymos and Dimorphos can be expected during the 30 days of observations [35].

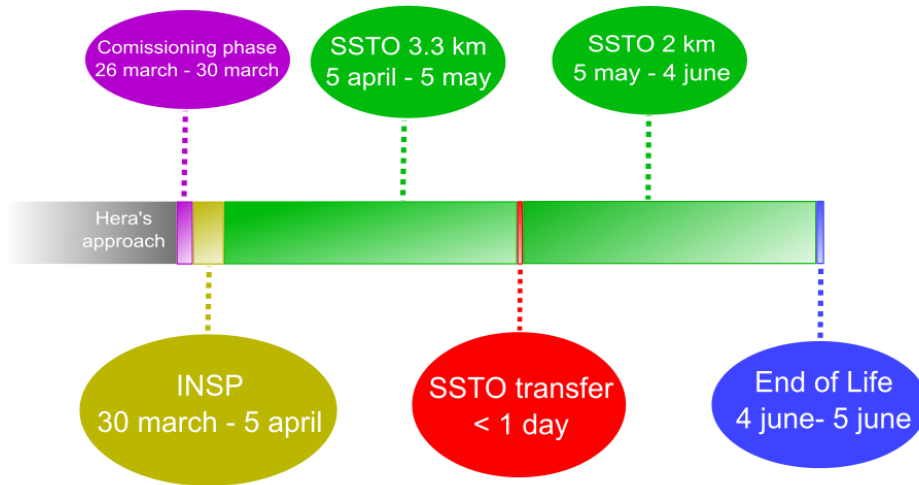


Figure 8: Timeline of the different phasis of Juventas.

**Transfer from SSTO 3.3 km to SSTO 2 km (TRFP) :** Once the observations are done, Juventas will maneuver and lower its orbit to finally come to a SSTO of 2 km of radius. The total  $\Delta V$  required is estimated at 3.7 cm/s.

**SSTO 2 km :** A new observation phase will begin similarly to the SSTO at 3.3 km. The combination of the coverage of the first observation phase and the second one leads to a 88% coverage of the surface of Dimorphos and 99.4% for Didymos.

**End of Life Phase - Landing on Dimorphos (EOLP) :** Once the coverage of Dimorphos is done, Juventas departs from the 2 km SSTO and attempts to land on Dimorphos with a relative impact velocity equal to or less than 10 cm/s. A series of maneuvers are done during the landing. The last one, called braking maneuver will be executed near the surface of Dimorphos to reduce the impact velocity and will have a major consideration during this thesis. During the descent, the onboard camera of Juventas will capture images of Dimorphos, and if possible, the DART impact site, enabling a better understanding of Dimorphos' surface properties. During the bouncing, Juventas utilizes its 3-axis gravimeter, accelerometer, and gyros to study the bouncing on the surface of Dimorphos. The collected data will allow to reconstruct the bouncing trajectory and determine the surface properties of the asteroid. If the spacecraft remains operational after landing, it can carry out its final science objectives, which involve studying the local gravitational field and the dynamical properties of Dimorphos during 30 days of observation.



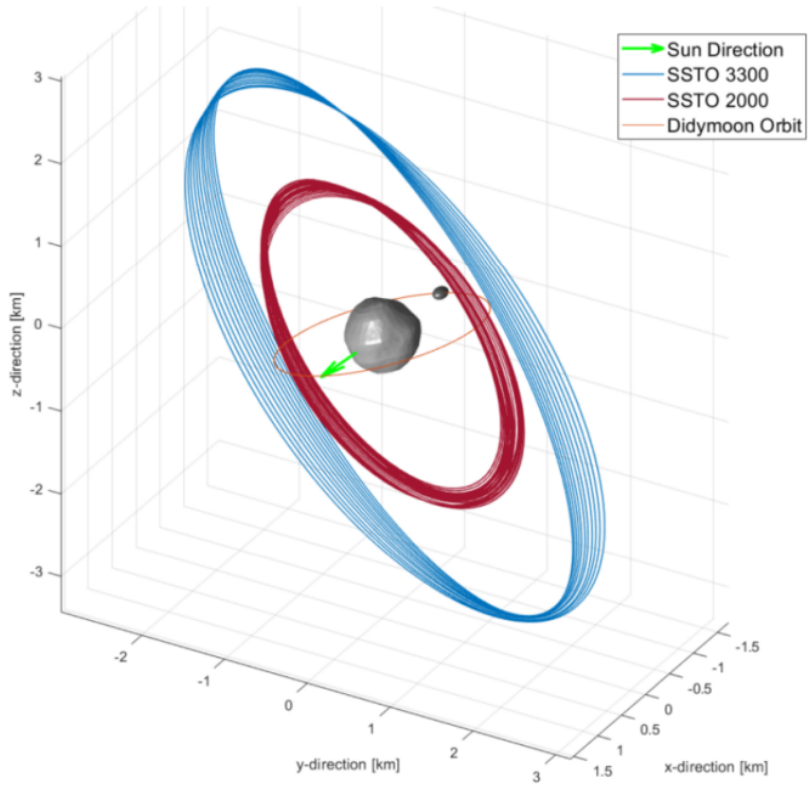


Figure 9: Representation of the different orbits adopted by Juventas [32].

## 2 Dynamic modeling

The main feature of a propagator is the definition of its dynamic, and the equations of motions that result of it. As such, this chapter shows how each physical feature is inserted inside the algorithm. A discussion about the different perturbations to consider is done, especially on the solar radiation pressure. Finally, the implementation of the braking maneuver is shown along with the initial conditions of the system.

### 2.1 Circular Restricted 3-Body Problem

Since the orbit of Didymos system is around 1.8 AU, it is relatively far from other celestial bodies. As such, only the gravitational pull from the primary and the secondary are considered, the perturbations from the Sun and the Earth are completely ignored. Since both are orbiting around each other with a very low eccentricity ( $<0.05$ ), the system will be approximated as a Circular Restricted 3 Body Problem (CR3BP).

The CR3BP consist of two mass  $m_1$  and  $m_2$  orbiting around a center of mass  $C_M$  with a constant separation. Here,  $m_1$  and  $m_2$  are Didymos and Dimorphos respectively. The third mass  $m$ , Juventas, is very low compared to the other two ( $\frac{m}{m_1} = 10^{-11}$   $\frac{m}{m_2} = 10^{-9}$ ) and its gravitational pull is not considered. Instead of using an inertial reference frame, a rotational frame (also called synodic frame)  $\mathcal{F} = \{\hat{\mathbf{e}}_r, \hat{\mathbf{e}}_\theta, \hat{\mathbf{e}}_z\}$  placed on the center of mass of the system and defined such as the masses  $m_1$  and  $m_2$  keep the same positions along the first axis. So  $\mathbf{r}_1 = r_1\hat{\mathbf{e}}_r$  and  $\mathbf{r}_2 = r_2\hat{\mathbf{e}}_r$  the positions of Didymos and Dimorphos relative to the center of mass respectively. The figure 10 shows the geometry of the system. Note that  $r_1 < 0$  since the origin of  $\mathcal{F}$  is at the barycenter.

The angular velocity of the frame is defined as  $\boldsymbol{\omega} = \omega\hat{\mathbf{e}}_z$  and the origin is set at  $C_M$ . The position of the satellite, in this case Juventas, is expressed as

$$\mathbf{r} = r_x\hat{\mathbf{e}}_r + r_y\hat{\mathbf{e}}_\theta + r_z\hat{\mathbf{e}}_z \quad (1)$$

The acceleration in  $\mathcal{F}$  is given by [40]

$$\ddot{\mathbf{r}} = (\ddot{r}_x - 2\omega\dot{r}_y - \omega^2r_x)\hat{\mathbf{e}}_r + (\ddot{r}_y + 2\omega\dot{r}_x - \omega^2r_y)\hat{\mathbf{e}}_\theta + \ddot{r}_z\hat{\mathbf{e}}_z \quad (2)$$

The gravitational force  $F_g$  on Juventas from the asteroids is expressed as

$$F_g = -Gm \begin{pmatrix} \frac{m_1}{\xi_1^3}(r_x - r_1) + \frac{m_2}{\xi_2^3}(r_x - r_2) \\ (\frac{m_1}{\xi_1^3} + \frac{m_2}{\xi_2^3})r_y \\ (\frac{m_1}{\xi_1^3} + \frac{m_2}{\xi_2^3})r_z \end{pmatrix} \quad (3)$$

with

$$\xi_i = \sqrt{(r_x - r_i)^2 + r_y^2 + r_z^2}$$

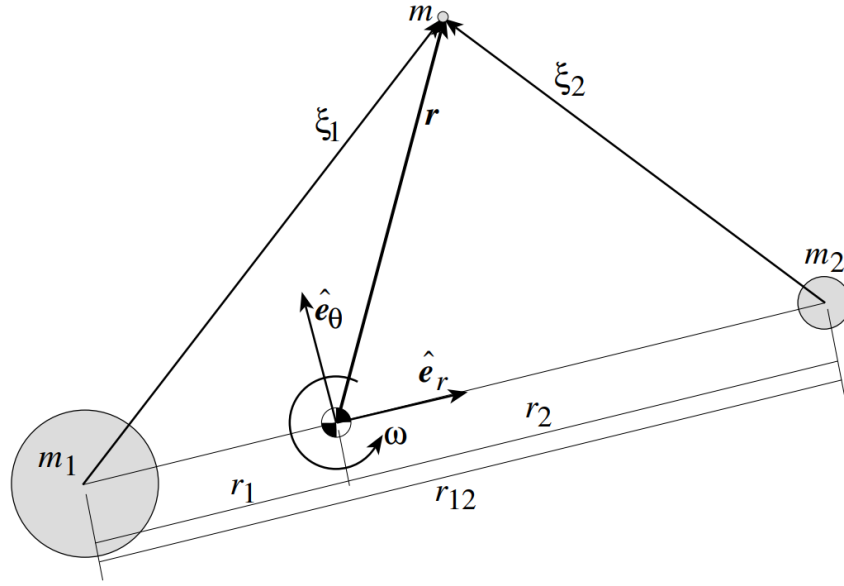


Figure 10: Illustration of the C3RBP from [34].

The Newton's second law gives then the acceleration

$$\ddot{\mathbf{r}} = \frac{\mathbf{F}_g}{m} \quad (4)$$

Inserting now (2) and (3) in (4), the equations of motion are finally given by :

$$\begin{cases} \ddot{r}_x - 2\omega\dot{r}_y - \omega^2 r_x + G \left( \frac{m_1}{\xi_1^3} (r_x - r_1) + \frac{m_2}{\xi_2^3} (r_x - r_2) \right) = 0 \\ \ddot{r}_y + 2\omega\dot{r}_x - \omega^2 r_y + \left( \frac{m_1}{\xi_1^3} + \frac{m_2}{\xi_2^3} \right) r_y = 0 \\ \ddot{r}_z + \left( \frac{m_1}{\xi_1^3} + \frac{m_2}{\xi_2^3} \right) r_z = 0 \end{cases} \quad (5)$$

## 2.2 Gravity perturbation

The model described previously considers each mass as points, which could be a good approximation for bodies with a shape close to a sphere. Nonetheless, this is not the case of Didymos and Dimorphos. It is why gravitational perturbations are added. To keep the simulation computationally efficient, the potential of each bodies is decomposed into spherical harmonics, and the gradient is retrieved to get the acceleration.

### 2.2.1 Gravity of Didymos

Since the satellite is propagating in empty space, the Laplace's equation  $\nabla^2 U = 0$  is respected. As such, the harmonics representations are obtained from solving Laplace's equation. Using

the spherical coordinates defined as :

$$\begin{cases} \xi_i = \sqrt{(r_x - r_i)^2 + r_y^2 + r_z^2} \\ \phi = \arcsin\left(\frac{r_z}{\xi_i}\right) \\ \lambda = \arctan\left(\frac{r_y}{r_x}\right) \end{cases} \quad (6)$$

The gravitational potential is then given by

$$U(\xi, \phi) = \frac{Gm_i}{\xi_i} \sum_{n=0}^N J_n \left( \frac{R_i}{\xi_i} \right) P_n(\sin \phi) \quad (7)$$

with  $P_n$  are the Legendre polynomial of degree  $n$ ,  $R_i$  is the radius of the sphere around the body  $i$  and  $J_n$  the harmonic coefficient of degree  $n$ .

Here, since the shape of Didymos is relatively close to a sphere, only the zonal perturbations are considered, up to the order 4. The coefficient used in this work are given by the company GMV [32] :

$$\begin{cases} J_2 = -0.011432722 \\ J_4 = 0.004583058 \end{cases} \quad (8)$$

The Legendre polynomials are given for  $x = \sin \phi = \frac{r_z}{\xi_1}$  by

$$\begin{cases} P_2 = \frac{1}{2}(3x^2 - 1) \\ P_4 = \frac{1}{8}(35x^4 - 30x^2 + 3) \end{cases} \quad (9)$$

The potential then becomes

$$U_1(\xi_1, \phi) = \frac{Gm_1}{\xi_1} \left( 1 + J_2 \left( \frac{R_1}{\xi_1} \right)^2 P_2(\sin \phi) + J_4 \left( \frac{R_1}{\xi_1} \right)^4 P_4(\sin \phi) \right) \quad (10)$$

with  $R_1 = 399$  m the diameter at the equator. Note that  $R_1$  is different from the mean radius of Didymos (387.5 m), since the shape is deformed at the equator.

The gravitational acceleration is then retrieved with :

$$\begin{cases} U_{1,x} = \frac{\partial}{\partial r_x} U(\xi_1, \phi) \\ U_{1,y} = \frac{\partial}{\partial r_y} U(\xi_1, \phi) \\ U_{1,z} = \frac{\partial}{\partial r_z} U(\xi_1, \phi) \end{cases} \quad (11)$$

### 2.2.2 Gravity of Dimorphos

Because the proximity of the satellite to Dimorphos during the propagation, and because the asteroid has an irregular shape, its model for the gravity should be more detailed. Instead of only considering the zonal perturbations, all harmonics will be considered up to the order 4.

$$\begin{array}{l|l} P_{2,0}(x) = \frac{1}{2}(3x^2 - 1) & P_{4,0}(x) = \frac{1}{8}(65x^4 - 30x^2 + 3) \\ P_{2,2}(x) = 3(1 - x^2) & P_{4,2}(x) = \frac{15}{2}(7x^2 - 1)(1 - x^2) \\ & P_{4,4}(x) = 105(1 - x^2)^2 \end{array}$$

Table 2: Legendre polynomials used in the equation 14.

Using the same coordinates retrieved using the equation 6, the gravitational potential is given by :

$$U(\xi_i, \phi, \lambda) = \frac{Gm_i}{\xi_i} \sum_{l=0}^N \sum_{m=0}^l \left( \frac{R_i}{\xi_i} \right)^l P_{l,m}(\sin \phi) \left( C_{l,m} \cos(m\lambda) + S_{l,m} \sin(m\lambda) \right) \quad (12)$$

with  $P_{l,m}$  the associated Legendre polynomials and  $R_i$  the distance from the center to the body  $i$ .

The matrix  $C$  and  $S$  are given by GMV [32] as :

$$C = \begin{pmatrix} 0 & 0 & 0 & 0 & 0 \\ 0 & 0 & 0 & 0 & 0 \\ -0.1325 & 0 & 0.0349 & 0 & 0 \\ 0 & 0 & 0 & 0 & 0 \\ 0.0429 & 0 & -0.0033 & 0 & 2.1810 \times 10^{-1} \end{pmatrix}, S = (0)_{5,5} \quad (13)$$

Since only the orders below or equal to 4 are considered, the expression of the potential becomes :

$$U(\xi_2, \phi, \lambda) = \frac{Gm_2}{\xi_2} \left( 1 + \sum_{l=1}^4 \sum_{m=0}^l \left( \frac{R_2}{\xi_2} \right)^l P_{l,m}(\sin \phi) C_{l+1,m+1} \cos(m\lambda) \right) \quad (14)$$

And the associated Legendre polynomials are shown in the table 2 The acceleration is then retrieved by computing the partial derivatives :

$$\begin{cases} U_{2,x} = \frac{\partial}{\partial r_x} U(\xi_2, \phi, \lambda) \\ U_{2,y} = \frac{\partial}{\partial r_y} U(\xi_2, \phi, \lambda) \\ U_{2,z} = \frac{\partial}{\partial r_z} U(\xi_2, \phi, \lambda) \end{cases} \quad (15)$$

### 2.3 Perturbed Circular-Restricted 3 body problem

Finally, inserting (15) and (11) in (5), the equation of motion is obtained :

$$\begin{cases} \ddot{r}_x = 2\omega\dot{r}_y + \omega^2 r_x - U_{1,x} - U_{2,x} \\ \ddot{r}_y = -2\omega\dot{r}_x + \omega^2 r_y - U_{1,y} - U_{2,y} \\ \ddot{r}_z = -U_{1,z} - U_{2,z} \end{cases} \quad (16)$$

This is the equation that will be solved numerically to compute the trajectory of the satellite.

## 2.4 Solar radiation pressure

The previous studies [32] [43] incorporated the solar radiation pressure in their work. Nonetheless, this thesis only focus on the bouncing of Juventas on Dimorphos, with time of propagation very short. Solar radiation pressure act only as a small perturbation in this case. Furthermore, it would induce additional computational time since the algorithm should take into account the geometry of Dimorphos along with position of the Sun has to be retrieved. It will be showed that this perturbation can be ignored with very limited consequences. The acceleration of the solar radiation pressure can be expressed as [26] :

$$a_{SRP} = -SRP_{1AU} C_r \frac{A}{m} \frac{1}{r_{AU}^2} \hat{r}_s \quad (17)$$

where  $SRP_{1AU} = 4.5 \cdot 10^{-6} \frac{N}{m^2}$  the solar pressure at 1 Astronomical Unit,  $C_r = 1.5$  the reflectivity coefficient,  $\frac{A}{m} = 1/30 \frac{m^2}{kg}$  the ratio between the effective cross section and the mass of the satellite,  $r_{AU}$  the distance of the satellite to the Sun and  $\hat{r}_s$  the vector towards the Sun. Since the gravity on the surface of Dimorphos is of the order of  $5 \times 10^{-5} \text{ m/s}^2$  which leads to a ratio between the solar pressure and the gravity of  $10^{-4}$ .

But simply comparing the different acceleration between the two forces is not enough. The perturbation due tot solar radiation pressure can become very relevant on the final position of the cubesat if it is applied on a long period. An analysis on the time of exposition has to be done. As it will be shown on the result section 6, the bouncing last rarely more than 2 hours. If we consider no eclipses, the maximum speed injected in the system is given by :

$$\Delta V = a_{SRP} \Delta t \quad (18)$$

where  $\Delta t = 2 \text{ h} = 7200 \text{ s}$ . The value obtained is  $\Delta V = 0.6 \text{ mm/s}$ , which is lower than the uncertainties on the incoming speed given by GMV. As such, the perturbation is considered as sufficiently low to be ignored.

## 2.5 Braking maneuver

The escape velocity from Dimorphos is  $8.4 \text{ cm/s}$  [4], a very low velocity that can be easily obtained from a bounce on the surface. It is why during the landing, a braking maneuver will be done in order to reduce the speed of the spacecraft. Previous studies [32] have already shown the huge importance of this maneuver on the success of the mission with a simpler model for bounces. According to the informations given by GMV, the time when the maneuver occurs is known, along with its intensity. Juventas will brake approximately at  $180 \text{ m}$  from the center of Dimorphos, by applying a  $\Delta V = 6.44 \text{ cm/s}$ . Since the propulsion is not instantaneous, it would be more accurate to implement it as an acceleration during a certain amount of time instead of simply change the velocity. The maximum force of propulsion of Juventas is  $1 \text{ mN}$  and it is assumed that the spacecraft has a mass of roughly  $12 \text{ kg}$  [35]. The maximum acceleration is then :

$$a_{max} = \frac{F}{m} = \frac{10^{-3} \text{ m}}{12 \text{ s}^2} \quad (19)$$

where  $F = 10^{-3}$  N the propulsion force of Juventas and  $m = 12$  kg the approximate mass.

This maneuver is applied in the opposite direction of the velocity. Since Juventas keeps its orientation during the braking in order for the instruments to work properly, the direction will be fixed during the entire maneuver. If we define  $\mathbf{v}_0$  the velocity of the spacecraft at the beginning of the brake and  $\ddot{\mathbf{r}}$  the acceleration vector from (16), the equations of motions become simply :

$$\ddot{\mathbf{r}}' = \ddot{\mathbf{r}} - a_{max} \frac{\mathbf{v}_0}{|v_0|} \quad (20)$$

To stop the brake when the  $\Delta V$  is reached, a check between each step of the propagation is done to ensure that no excessive acceleration is performed.

Note that a way to improve this implementation of the braking maneuver would be to use the rocket equation. Nonetheless, the above method was preferred to keep the propagation simpler since the consumption of Juventas and the quantity of fuel still in the tank at the beginning of the maneuver are not precisely known.

### 3 Modeling of Bouncing Motion

This chapter explains how the bounces of the satellite is included in the simulation. First, the way the collision is detected is described, then the 3D model of Juventas and the physical interactions are shown. Finally, it explains how the bouncing model is implemented in the propagator.

#### 3.1 Surface collision

During the propagation, the algorithm has to detect when the cubesat hits the asteroid. To do so, a mathematical representation of the surface of Dimorphos is used. It is very common in the simulation of small bodies to use shape model, which are 3D bodies defined by triangles arranged to define the geometry of the object. Each facet contains a face center and a unitary normal vector. The figure 11 shows the shape model of Dimorphos used in the thesis [11]. A particularity of the system is the synchronicity between the rotation of Dimorphos and its orbit. As a consequence, the orientation of the secondary stays the same in the rotational frame and does not need to be adjusted during the propagation.

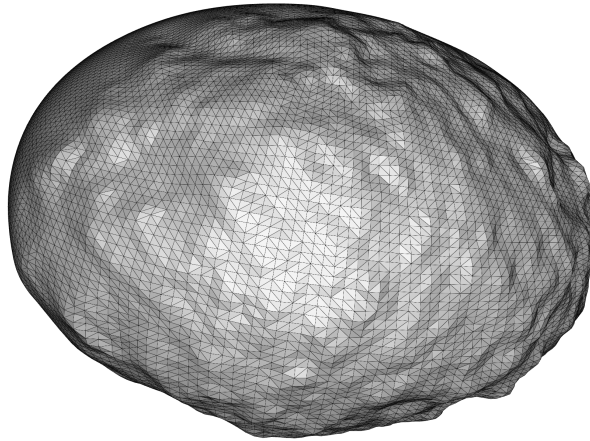


Figure 11: Shape model of Dimorphos used in the thesis [11].

In previous studies [32], a very simple model was used, consisting of a point bouncing similarly as a ball on a flat surface. The satellite was propagated until the distance from the satellite to the center of any facet is inferior to a certain threshold (usually 15 m). This makes the bounces very inaccurate since each facet trigger an impact when Juventas approach in a spherical area around the facet. A lot of issues found by this approximation, especially geometrically. The satellite tended to bounce far away from the surface, which could lead to a very odd prediction for simulations with very complex shape models (see figure 12). Also, the bounces can be



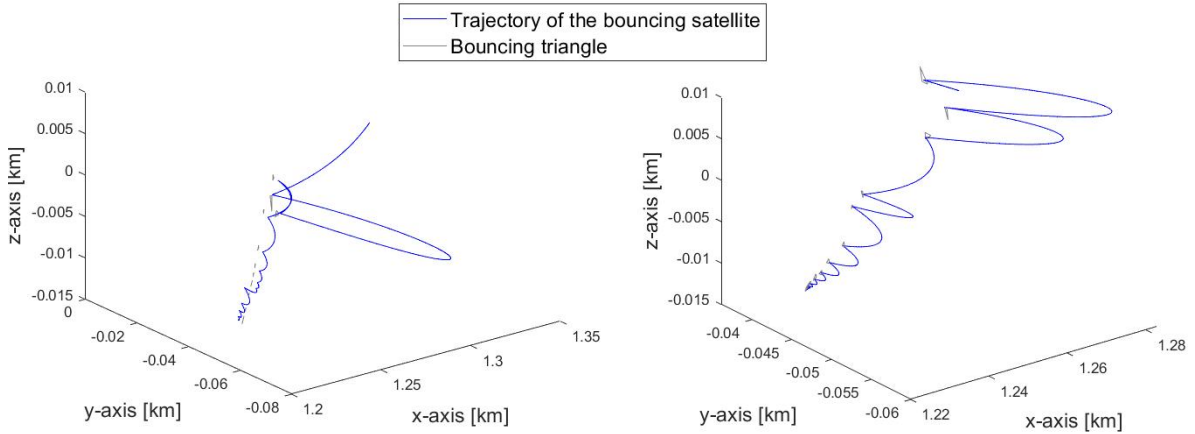


Figure 12: Graphs showing the trajectory of the satellite and the triangle considered by the propagator for the bounding. Left : Trajectory with the surface collision from [32]. Clearly, the trajectory does not fit to the facets. Right : Trajectory with the new surface collision. Here the trajectory fits much better to the facets. Also, it induces a totally different trajectory, showing the importance of the new collision system.

computed on the wrong facets, and produce inaccurate direction after the bounce.

To locate the impacts with accuracy, a new method for collision detection has been implemented. As such, we define  $S$ ,  $F$  and  $\mathbf{n}$  the satellite position, the face center and the normal vector respectively (see figure 13). The propagator is set to stop when the following condition is fulfilled :

$$\mathbf{FS} \cdot \mathbf{n} \leq 0. \quad (21)$$

Where  $\mathbf{FS}$  is the vector from the point  $F$  to  $S$ . This notation will be used during the entire thesis to describe the vector between 2 points.

Nonetheless, this method requires to choose carefully the landing facet. To do so, the algorithm needs to guess at each step which is the triangle the most susceptible to lie along the trajectory of the satellite. First, the code looks at the closest face center, but it is not enough because a collision could occur on a different facet. To increase the accuracy, the algorithm developed uses a line parallel to the velocity vector and passing through the position of the satellite, called the detection ray. Let's call  $A$ ,  $B$  and  $C$  the 3 points of the facet. First, the intersection  $I$  between the detection ray and the plane formed by the facets is retrieved (see figure 13). Now, the algorithm checks if  $I$  is inside the triangle. This can be easily done using the next condition :

$$\text{sign}\left(\mathbf{n} \cdot (\mathbf{AI} \times \mathbf{AB})\right) = \text{sign}\left(\mathbf{n} \cdot (\mathbf{BI} \times \mathbf{BC})\right) = \text{sign}\left(\mathbf{n} \cdot (\mathbf{CI} \times \mathbf{CA})\right) \quad (22)$$

Each term changes its sign depending on which side the point  $I$  is from the lines  $AB$ ,  $BC$  and

CA. When all the values are either 1 or -1, I is inside the triangle. If this condition is fulfilled, then the algorithm checks the condition 21 using the parameters of the facet. Otherwise, it looks at the second closest triangle, then the third etc. If the sixth facet is still negative, the propagation just continues.

The computational time is dependent on the number of facets to retrieve the distance from. With the shape model in figure 11, the mean time is 3 ms.

This method can fail if the normal is not set on the right direction. Indeed, a normal point towards the center of the asteroid would lead to a collision without touching the surface. Also, this method requires the use of a numerical method with variable step to avoid any overshoot inside the surface and to reduce the number of checks for collisions has to be made.

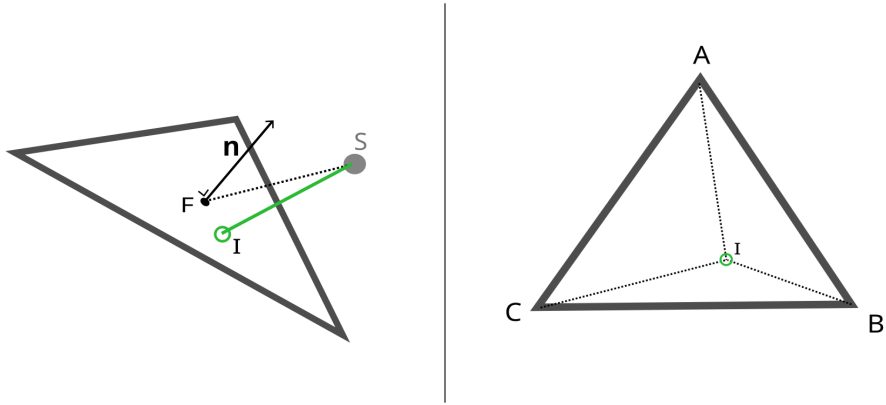


Figure 13: Left : Scheme of the parameters used for the collision condition. Right : Scheme of a facet, checking if the point I is inside the triangle.

### 3.2 Point-Like Bouncing Model

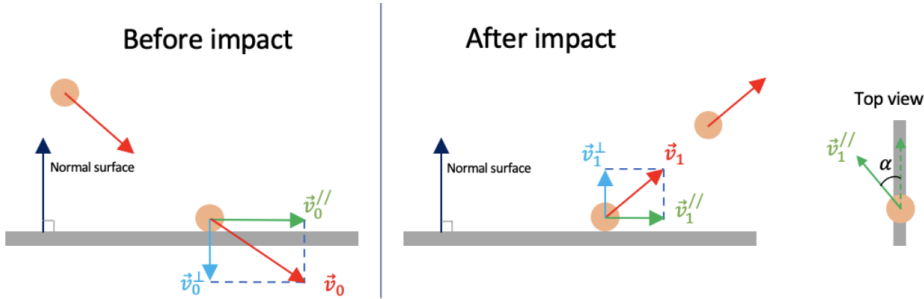


Figure 14: Scheme of the point-like bouncing model [32].

A first bouncing model was considered in the thesis of Guillaume Roisin [32], with a very simple implementation. The satellite is considered as a point object with a velocity vector  $v_1$ .

When a bounce occurs on a facet, the normal vector  $\mathbf{n}$  is retrieved. The normal velocity  $\mathbf{v}_1^\perp$  and the tangential velocity  $\mathbf{v}_1^\parallel$  are computed as :

$$\mathbf{v}_1^\perp = (\mathbf{v}_1 \cdot \mathbf{n}) \mathbf{n} \quad (23)$$

$$\mathbf{v}_1^\parallel = \mathbf{v}_1 - \mathbf{v}_1^\perp \quad (24)$$

The bouncing is then defined using 2 constants, the normal coefficient of restitution  $e$  and the tangential coefficient of restitution  $f$ . To get the velocity after the bounce, the next formulas are used :

$$\mathbf{v}_2^\perp = e |\mathbf{v}_1^\perp| \mathbf{n} \quad (25)$$

$$\mathbf{v}_2^\parallel = f \mathbf{v}_1^\parallel \quad (26)$$

This simple bouncing model is easy to implement and has been used to check the validity of the code.

### 3.3 3D Bouncing Model

The previous model was very simple and easy to emulate through a simulation. Nonetheless, it is absolutely not representative of the satellite, since we are considering it as a point for the bounce. This point-like model has a major issue since it does not account for the rotation of the satellite. A major improvement of this thesis is a new model, with a 3D shape for Juventas, and the addition of 3 new degree of freedom for the rotation of the satellite. For this purpose, we use a toolbox on Matlab named Simscape Multibody [36].

#### 3.3.1 Physics engine

The physics engine of the toolbox is based on the work of Brian Vincent Mirtic, "Impulse based Dynamic Simulation of Rigid Body System" [27]. Since the design of a physics engine is a very complex matter and a large domain, only the main features will be explained.

First, the system defines an inertial world frame. Since the impact of the virtual forces on the rotations of the spacecraft are negligible, they won't be accounted during the contact. It also means that the system is no longer in a synodic frame during the simulation inside the toolbox. Each body in the system is defined by a frame  $F$  associated to it, with 4 parameters. A position vector, velocity vector, a quaternion for the orientation and a rotation vector. We will denote the parameters of the frame :

$$\mathbf{X}_F = \begin{pmatrix} \mathbf{x} \\ \mathbf{v} \\ \mathbf{q} \\ \boldsymbol{\omega} \end{pmatrix} \quad (27)$$

This frame follows the body during the entire simulation. With a geometry given by a set of  $n$  vectors called vertices  $\mathbf{a}_i$  with  $i = 1, 2, \dots, n$ . As such, each point of the object can be located in the world frame using

$$\mathbf{r}_i = \mathbf{x} + R(\mathbf{q})\mathbf{a}_i \quad (28)$$

with  $\mathbf{r}_i$  the position of the vertice in the world frame and  $R(\mathbf{q})$  the rotation matrix associated to the quaternion  $\mathbf{q}$ .

The motion of the frame is given by the equation :

$$\dot{\mathbf{X}}_F = \begin{pmatrix} \dot{\mathbf{x}} \\ \dot{\mathbf{v}} \\ \dot{\mathbf{q}} \\ \dot{\boldsymbol{\omega}} \end{pmatrix} = \begin{pmatrix} \mathbf{v} \\ \mathbf{g}(\mathbf{x}) + \mathbf{F}_e/m \\ \frac{1}{2}\mathbf{q} * \mathbf{Q}(\boldsymbol{\omega}) \\ I^{-1}\mathbf{M} + I^{-1}\boldsymbol{\omega} \times I\boldsymbol{\omega} \end{pmatrix} \quad (29)$$

where  $\mathbf{g}(\mathbf{x})$  the gravity acceleration vector,  $\mathbf{F}_e$  the external force (except gravity) applied to the body,  $m$  its mass,  $*$  the quaternion product,  $\mathbf{Q}(\boldsymbol{\omega}) = \omega_x i + \omega_y j + \omega_z k$  where  $i, j$  and  $k$  are the basis elements of the quaternion space,  $\mathbf{M}$  the moment of inertia applied to the object and  $I$  its moment of inertia. The dynamics of the rotation vector is given by the Euler equations and is defined the frame of the body. For more information about quaternions and Euler equations, the appendix has a section on them (quaternion 8.4, Euler equation 8.4).

### 3.3.2 Contact Force

Now that we know the equations of motion, we can determine the forces applied to the different objects. As such, we want to model the contact between a rigid body and a surface. To do so, Simscape multibody uses a penalty method, based on a damping-spring contact [16]. This method allows for the different object to penetrate each other a little bit, and apply a force depending on the penetration depth.

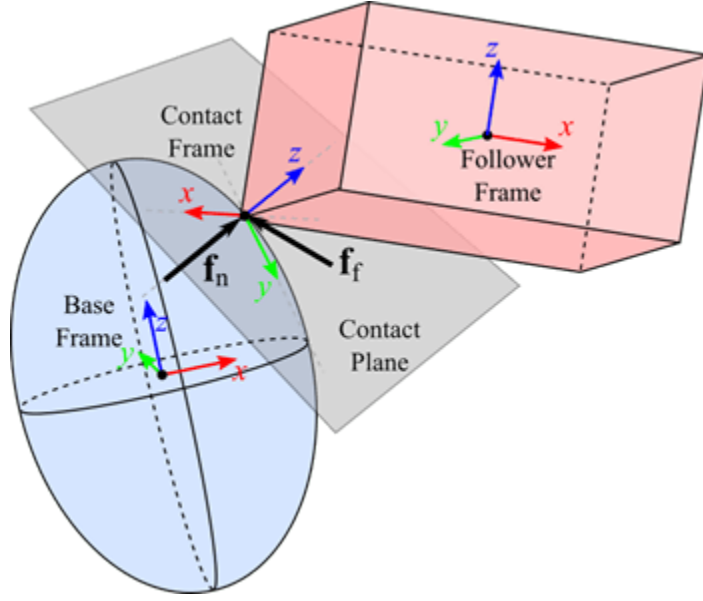


Figure 15: Scheme of the contact between 2 rigid bodies [16].

The normal force is given by

$$\mathbf{f}_n = s(d, l)(k \cdot d + \Gamma \cdot d') \quad (30)$$

where  $d$  the penetration depth,  $d'$  its derivative,  $k$  the stiffness constant,  $\Gamma$  the damping coefficient and  $s(d, l)$  a smoothing function varying from 0 to 1 when  $d < 0$  and  $d > l$  respectively.  $l$  is called the transition region, it assures the continuity between a regime where the force is null ( $d < 0$ ) and when it's maximal ( $d > l$ ) and avoid abrupt changes. The normal force is defined as positive, and is always perpendicular to the contact plane.

Nonetheless, the friction between the different bodies has to be modeled. To do so, the engine uses the stick-slip method considering 2 regimes of friction, a static one and a dynamic one. Other models were good candidates for the friction ([2][44][29][33]) but this is the only one implemented in simscape multibody. This one has the advantage to be easily computed and gives an instantaneous force of friction, as opposite to models based on coefficients of restitution. It is defined according to the normal force :

$$\mathbf{f}_f = \mu(v_{\parallel}, v_c, \mu_s, \mu_d) \mathbf{f}_n \quad (31)$$

with  $\mu(v_{\parallel}, v_c, \mu_s, \mu_d)$  a function giving the coefficient of friction according to several parameters.  $\mu_s$  and  $\mu_d$  are the coefficient of static friction and dynamic friction respectively,  $v_{\parallel}$  is the norm of the velocity of the contact point parallel to the contact plane and  $v_c$  the critical speed.  $\mu$  is defined as 0 in  $v_{\parallel} = 0$  and until reaching the critical velocity, which is the speed at which the coefficient is maximum and reach the static coefficient of friction. When this threshold is passed, the  $\mu$  decreases slowly and tends towards the dynamic coefficient of friction  $\mu_d$ . The figure 16 shows the profile of the coefficient of friction.

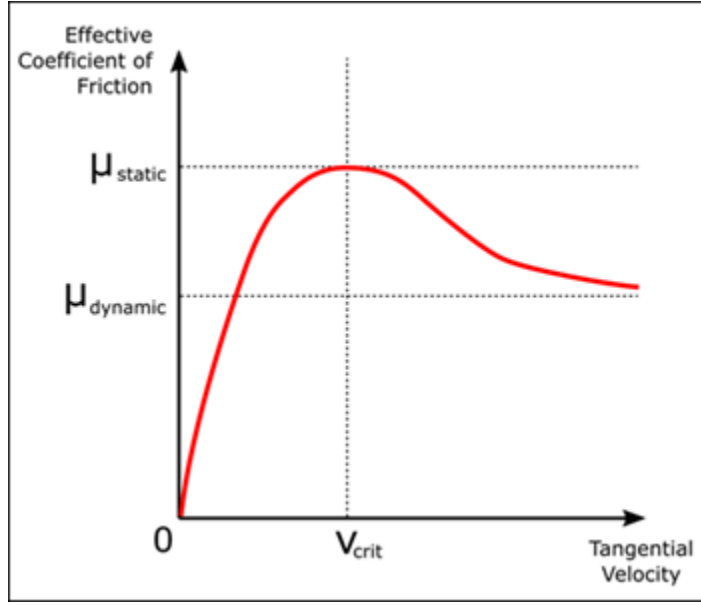


Figure 16: Evolution of  $\mu$  as a function of the tangential velocity [16].

Different parameters are used in this model for the contact force, but some are only present for numerical purpose. The others have to be carefully to achieve the most realistic simulation possible. The higher  $k$ , the less penetration will be allowed at a higher computational cost. The default value in the literature [25] is  $10^6$  N/m. Since Juventus is only of the order of 10 kg and the gravity of Dimorphos is very weak, this value is kept and gives very low contact time. On the other hand,  $l$  has to be as small as possible to be accurate since the surface considered are rigid. The default value is  $10^{-4}$  m.  $v_c = 10^{-3}$  m/s was kept for the same reasons. Of course, to fix correctly these values, an experiment should be done but it does not enter the scope of the thesis, it is very complex to conduct this kind of test in laboratory. Even if some works on the subject exist [41], it was never done under such extreme conditions as Dimorphos. As such, the simulation is only valid in the frame of this study.

The only relevant parameters left are  $\Gamma$ ,  $\mu_s$  and  $\mu_c$ . The damping coefficient  $\Gamma$  directly affects the energy returned by the surface to the satellite, and is probably the major factor characterizing the bounce. As seen on [5], the coefficient of restitution, defined as the ratio between the speed after and before the bounce, of the asteroid can be high, the value of 0.8 has been measured for the Hayabusa mission on the asteroid Itokawa [6]. Nonetheless, the link between the damping coefficient and coefficient of restitution is not clear. An heuristic demonstration has been made in the appendix (8.4). The 2 coefficients of friction  $\mu_s$  and  $\mu_c$  on the other hand will mainly affect the transfer of energy through the rotation of the body. Again, the link between coefficients of restitution and the coefficient of friction is not straightforward. An experiment from Stefaan Van wal and Onur Çelik [41] retrieved the coefficients of restitution and the coefficient of friction according to the Stronge's model, but the results were very random and showed no clear dependencies with impact conditions. Considering that most of

Symbol	Parameters
$d$	Computed
$d'$	Computed
$l$	$10^{-4}$ m
$k$	$10^6$ N/m
$\Gamma$	Chosen from 40 to 4000
$\mu_s$	Chosen from 0.3 to 0.8
$\mu_c$	$0.5 \times \mu_s$
$v_{\parallel}$	Computed
$v_c$	$10^{-3}$ m/s

Table 3: Summary of the different parameters used to compute the contact force.

small bodies are composed of carbon, we will take as a range for  $\mu_s$  from 0.3 to 0.8. The choice of  $\mu_c$  is not determined and dependant on the properties of the surface, nonetheless adding a new variable would increase the computational cost for further analysis. As such,  $0.5 \times \mu_s$  is picked.

### 3.3.3 Geometry

The geometry of the CubeSat is relatively simple, and is decomposed through rigid boxes of different sizes. The main body has a shape of  $100 \times 365.9 \times 226.3$  mm [7]. Concerning the solar panels, as seen on the figure 17, they are in three parts and joined by different hinges. Each plate will be modeled as a box of  $297 \times 10 \times 270$  mm placed next to each other. The mechanical system allows the spacecraft to rotate the solar panels to face the sun. Nonetheless, this study will only consider fixed position for the solar panels, as represented on the figure 17. Note that the CubeSat will land on the  $+Z$  direction.

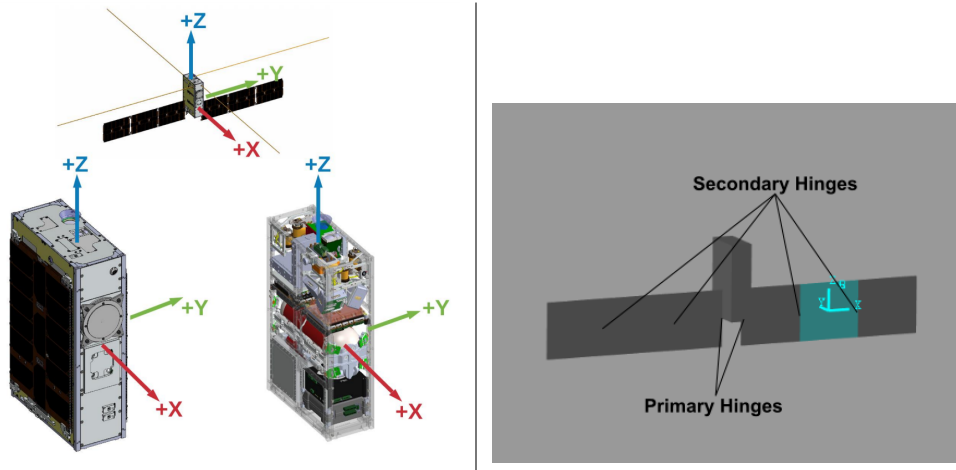


Figure 17: Left : Mechanical view of Juventas [7]. Right : Modeling inside Matlab, a solar panel is highlighted in blue.

Feature	Primary	Secondary
Wire diameter	0.51 mm	0.5 mm
Inner diameter	4.45 mm	3.5 mm
Max Torque	21.1 Nmm	19 Nmm
Max Torsion Angle	225.4 °	294 °
Leg Length	19.05 mm	6.5 mm

Table 4: Characteristics of the hinges given by the manufacturers [39] [1].

### 3.3.4 Hinges

The primary hinges are composed of Febrotec 0T020-270-093 [39], and the secondary hinges are Lesjofors 7017: TSR 0,5X3,5X3X12 [1] between each solar panel, as illustrated on the figure 17. As such the characteristics given by the manufacturers are given in the table 4.

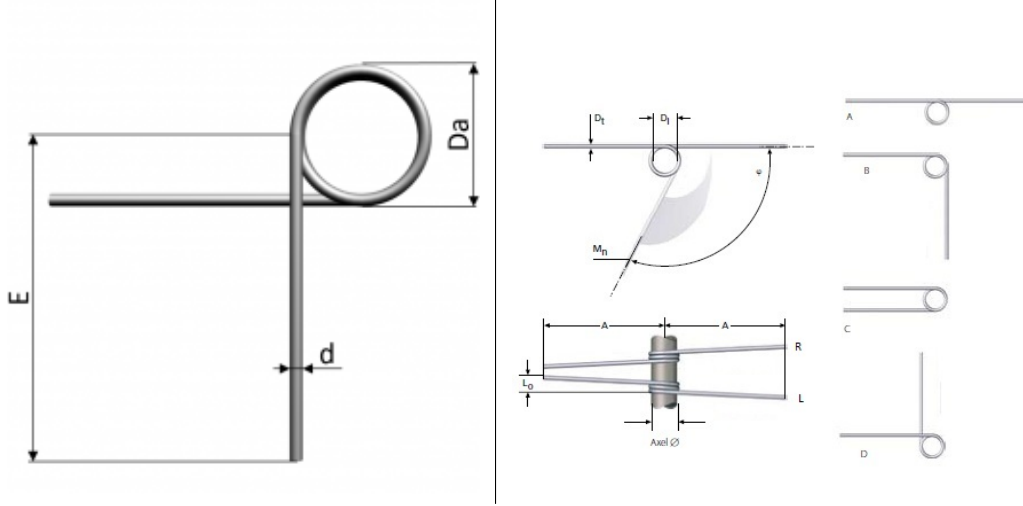


Figure 18: Left : Primary hinge [39]. Right : Secondary hinge [1].

Simscape multibody allows to use different joints to apply forces between bodies. As such, a revolute joint is used to link each part of the geometry, adding a new constraint on the motion on the joint and a rotational degree of freedom. The torsion produced by the joint is given by

$$T = -k_T(\theta - \theta_0) - \Gamma_T\dot{\theta} \quad (32)$$

where  $k_T$  is the torsional stiffness constant,  $\Gamma_T$  the torsional damping constant,  $\theta$  the angle of the joint,  $\dot{\theta}$  its first derivative and  $\theta_0$  the equilibrium angle.



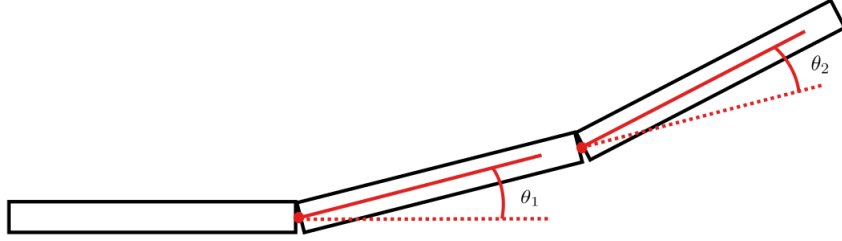


Figure 19: Schematic view of the joint in the solar panels.

Choosing the different constants is a hard task to assure a good emulation of the hinges. The literature has already some resources about the flexibility of deployment mechanisms ([20] [45] [28]). Furthermore, this model is linear and may not be representative of the true behavior of the spring in the hinges. Indeed, if too much force is applied, the deformation is non-elastic and the resultant force becomes non-linear. Nonetheless, the mass and the gravity of Dimorphos are very low, the torque applied to the solar panels should be limited in these conditions. It is why this approximation is used. To be sure of having constants in an elastic regime, a limite of  $180^\circ$  is set for the joints. This gives a constant  $k_T = 21.1/180 = 0.117 \text{ Nmm}/^\circ$  for the primary and  $k_T = 0.106 \text{ Nmm}/^\circ$  for the secondary. The  $\Gamma_T$  is fixed at 1/10 of the stiffness constant. Since each spring is present 2 times between the hinges, the final constant values for the joint are given in the table 5.

Primary joint	$k_T = 0.234 \text{ N mm}/^\circ$	$\Gamma_T = 0.0234 \text{ N mms}/^\circ$
Secondary joint	$k_T = 0.212 \text{ N mm}/^\circ$	$\Gamma_T = 0.0212 \text{ N mms}/^\circ$

Table 5: Table of the constant used for the joints.

### 3.3.5 Stop condition

During the propagation of the bouncing, the condition to stop it has to be set up. 2 cases have to be taken into account :

- Juventas bounces off Dimorphos or orbits around it
- Juventas bounces until it comes at rest

For the first case, it is relatively hard to deduce. A solution could be to insert an area around Dimorphos and considering the satellite as lost if it propagates out of it. The issue is to fix the dimensions of this area. Placing this boundary too close to the surface leads to false bounce off that could compromise the data. If set too high, the algorithm could run eternally if the satellite goes into a closed orbit or an escape trajectory. Instead, a time limit is set and the

propagation stops if the time limit is passed. Again, too low would stop the propagation too early and too long would induce a high computational cost. After some tests, 12 h appeared to be a reasonable time to allow even the biggest bounces to touch the ground.

The second case is more tricky. The velocity of the satellite is technically never 0, but a threshold can be set up to consider the satellite at rest. If the norm of the after bounce velocity  $\mathbf{v}_{\text{out}}$  is less than 0.5 mm/s, the bounce stops and the algorithm considers that Juventas has landed. A particular case can happen, if the satellite bounces with a relatively high incidence angle, it can slide on the surface. To avoid this phenomenon, another stop condition is added :  $\mathbf{v}_{\text{out}} \cdot \mathbf{n} < 0.5$  mm/s with  $\mathbf{n}$  the normal unitary vector of the facet. Doing so, if the satellite bounces with a relatively high velocity, but a normal component that is too weak, the propagation is stopped and Juventas is considered as landed.

The satellite can also slide on the surface. To stop the propagation when it occurs, a last stop condition is set, with  $|v_{\text{out}}| < 1$  mm/s. As such, the satellite is allowed to slide on the surface but will be considered at rest when its velocity is too slow.

### 3.3.6 Overall implementation

Now that the different elements composing the bounce are well defined, they have to be assembled accordingly with the propagator to have the most realistic simulation as possible. Since the only physical contact happens only during the bounce, and for computational time reason, the physics engine will be used only during the contact between the satellite and Dimorphos. In fact, the algorithm is composed of 5 phases, illustrated in the Figure 20.

1. The satellite is propagated respectively to the dynamic of the system. At each step, the code checks if a collision occurs.
2. When a collision occurs, the propagator is stopped and 2 cases are possible. If the stop condition is fulfilled, the simulation is stopped. Otherwise, the velocity, orientation and rotational speed of the satellite are collected, along with the parameters of the landing facet.
3. The collected parameters are transformed in the frame of the facet and put inside the physics engine. The physics engine runs until the satellite touches the flat ground, but an extra margin of 50 s is given since the satellite can hit the ground multiple times. This step usually takes less than 4 seconds.
4. The same data are collected and transformed into the general frame, the propagation then continues with the new velocity.
5. The code goes back to the phase 1, until the stop condition is fulfilled or if the propagation lasts for more than 12 hours.

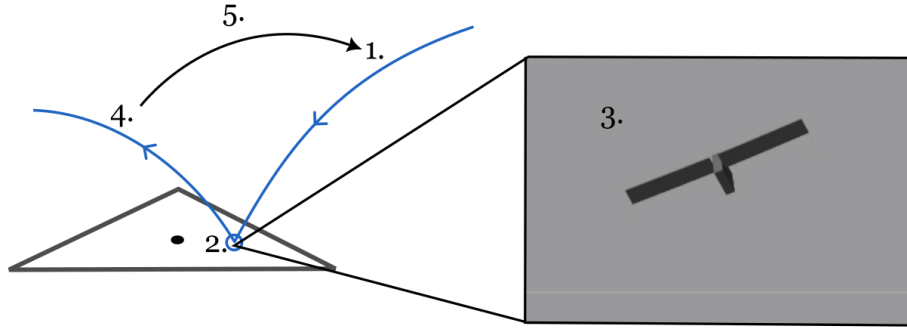


Figure 20: Scheme of the different phases.

### 3.3.7 Physics Engine Solver

Simscape multibody is able to use several numerical methods for its simulations. This work requires a good compromise between computational time and accuracy. As such, a variable step method is used, the Dormand-Prince method [19]. The relative error is set to  $10^{-5}$  and the absolute error to  $10^{-6}$ . It reduces the simulation for one bounce to few seconds and allows a study on a big number of samples.

### 3.3.8 Free rotation

During the propagation, the satellite continues to rotate. Since using the physics engine requires a time of compilation, it is time consuming to use it for the rotations between bounces. Furthermore, the propagation can last for hours before it stops. To propagate the position, but also the orientation, simple dynamic equations are used.

Since the object is not subject to any torque, the Euler equations are simplified and the equations to solve are :

$$\dot{\mathbf{q}} = \frac{1}{2} \mathbf{q} * \mathbf{Q}(\boldsymbol{\omega}) \quad (33)$$

$$\dot{\boldsymbol{\omega}} = I^{-1} \boldsymbol{\omega} \times I \boldsymbol{\omega}. \quad (34)$$

The time between 2 bounces is retrieved from the propagator, then  $\mathbf{q}$  and  $\boldsymbol{\omega}$  are computed numerically. Proceeding like this allows the algorithm to gain much more time and propagating several satellite landing models.

## 4 Numerical Method

The context of the study requires a careful the numerical method for the propagator. The previous work [32] developed an algorithm using the Runge-Kutta Fehlberg method. Nonetheless, it was used for landing analysis and does not account for the bouncing of Juventas. Here in this chapter, the method will be explained along with the implementation of the bouncing model to produce an algorithm able to propagate a big number of satellite. The chapter will conclude with a discussion about the validity and the performances of the algorithm.

### 4.1 Runge-Kutta Fehlberg

The Runge-Kutta Fehlberg method is a numerical method with a variable step, computed according to an allowed error. This feature gives 2 main advantages compared to fixed time step methods:

- There is no need to choose carefully a time step
- The propagator runs faster when the iterations are easy to compute

To compute the error, 2 approximations of order 4 and 5 are compared. The time step is reduced until the required error is achieved.

0						
1/4	1/4					
3/8	3/32	9/32				
12/13	1932/2197	-7200/2197	7286/2197			
1	439/216	-8	3680/513	-845/4104		
1/2	-8/27	2	-3544/2565	1859/4104	-11/40	
	16/135	0	6656/12825	28561/56430	-9/50	2/55
	25/216	0	1408/2565	2197/4104	-1/5	0

Table 6: Butcher tableau.

From the table 6, the different coefficients are defined as :

$$k_1 = f(t_n, y_n) \quad (35)$$

$$k_2 = f\left(t_n + \frac{1}{4}h, y_n + \frac{1}{4}k_1\right) \quad (36)$$

$$k_3 = f\left(t_n + \frac{3}{8}h, y_n + \frac{3}{32}k_1 + \frac{9}{32}k_2\right) \quad (37)$$

$$k_4 = f\left(t_n + \frac{12}{13}h, y_n + \frac{1932}{2197}k_1 - \frac{7200}{2197}k_2 + \frac{7286}{2197}k_3\right) \quad (38)$$

$$k_5 = f\left(t_n + h, y_n + \frac{439}{216}k_1 - 8k_2 + \frac{3680}{513}k_3 - \frac{845}{4104}k_4\right) \quad (39)$$

$$k_6 = f\left(t_n + \frac{1}{2}h, y_n - \frac{8}{27}k_1 + 2k_2 - \frac{3544}{2565}k_3 + \frac{1859}{4104}k_4 - \frac{11}{40}k_5\right) \quad (40)$$

The 2 approximations for the are defined as :

$$y_{n+1} = y_n + \frac{16}{135}k_1 + \frac{6656}{12825}k_3 + \frac{28561}{56430}k_4 - \frac{9}{50}k_5 + \frac{2}{55}k_6 \quad (41)$$

$$y_{n+1}^* = y_n^* + \frac{25}{216}k_1 + \frac{1408}{2565}k_3 + \frac{2197}{4104}k_4 - \frac{1}{5}k_5 \quad (42)$$

Then, for the error, the norm between the 2 results is computed :

$$\epsilon = |y_{n+1} - y_{n+1}^*| \quad (43)$$

The time step is chosen depending on the error evaluated. A threshold  $\epsilon_0$  representing the maximum allowed error is chosen and depending if  $\epsilon$  is greater or lower to this value, the time step becomes lower or greater respectively :

$$h = \begin{cases} 0.9 h(\frac{\epsilon_0}{\epsilon})^{1/5} & \text{if } \epsilon \geq \epsilon_0 \\ 0.84 h(\frac{\epsilon_0}{\epsilon})^{1/4} & \text{if } \epsilon < \epsilon_0 \end{cases} \quad (44)$$

Note that even if  $\epsilon = \epsilon_0$ , the time step is reduced to assure that even by using approximations, the error is lower than the maximum allowed error.

## 4.2 Time step reduction on the surface

The timestep is computed according to the error  $\epsilon$ , but is not accounting for the collision of the surface. As such, the algorithm needs a mechanism to stop the propagation accurately on the surface. Indeed, a too big time step could bring the particle to stop inside Dimorphos, and the bouncing trajectory would have odd behavior, or even continuing to bounce inside the shape model.

To do so, when  $y_{j+1}$  meets a stop condition (as defined in the section 3.3.5), the propagation is stopped. A new check is done :

$$\mathbf{n} \cdot (\mathbf{r}_{j+1} - \mathbf{F}) \leq d_n \quad (45)$$

where  $d_n$  is the maximum penetration depth allowed for the propagation,  $\mathbf{F}$  the face center of the bouncing face,  $\mathbf{n}$  the normal of the facet and  $\mathbf{r}_{j+1}$  the position of the spacecraft at the step  $j + 1$ .

If the condition is fulfilled, the value  $y_{j+1}$  is saved and the particle is considered as it has collided. On the other hand, the condition is not met, the time step is divided by 2 and  $y_{j+1}$  is computed again. The propagation goes on until the stop conditions and (45) are met.

Modifying the time step at proximity of the surface is a good way to stop the propagation on the surface without adding more complexity to the algorithm.

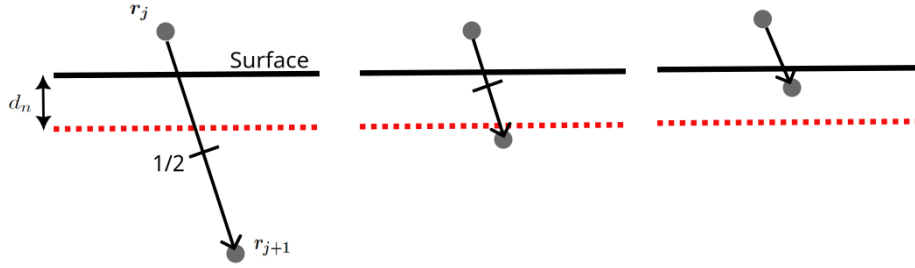


Figure 21: Representation of the time step reduction on a surface.

### 4.3 Vectorization

To improve the efficiency of the algorithm, a vectorization can be applied to the code. Instead of computing each propagation one by one, they are all computed in parallel.

Let's define  $y_j^i$  the position and velocity vector of the satellite  $i$  at the step  $j$ . At the beginning of the propagation, the time step  $h_i$  is computed for the next iteration of  $y_j^i$ , as described previously. Each  $y_{j+1}^i$  is retrieved and registered in a big matrix of results. Next, a check up is set to see if a collision occurs (see section 3). If yes, the index corresponding to the stopped satellite is ignored for the rest of the propagation. It can be achieved easily using logical arrays in Matlab. As such, an array  $l$  is defined, composed with only 1 and 0. It determines if a satellite is still ongoing or stopped. Then,  $h_i$  is actualized and another iteration goes on. This process lasts until the entire array  $k$  is equal to 0.

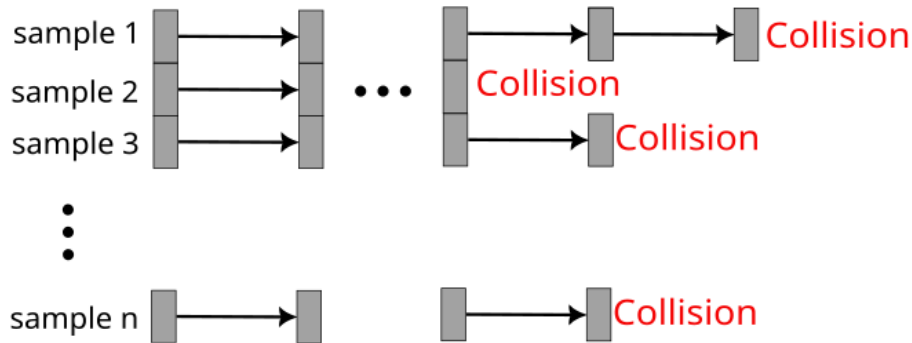


Figure 22: Scheme of the vectorization.

### 4.4 Implementation of the bouncing motion

Since the vectorization is only used for the propagation of the satellite, the bouncing has to be included carefully to obtain the most realistic result as possible.

As such, the code begins by a propagation of each satellite. When it is done, the velocity, the

orientation and the rotational speed are retrieved. Then begins the bouncing computation, several simulations are done inside simscape multibody to compute the motion of each particle.

Once the simulations are done, a check for the stop conditions is done. Another logical array  $k$  is defined to determine which particle is still bouncing or not. According to the result of the check,  $k$  is actualized.

The different parameters of the satellite after the bounce (velocity, attitude, rotational speed) are extracted and used to continue the propagation. This process lasts until every particles have landed.

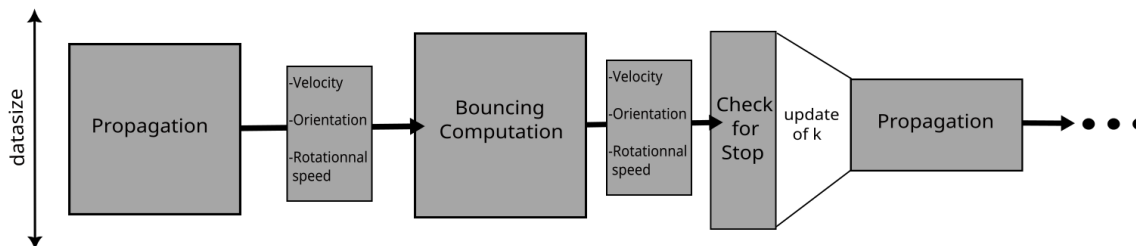


Figure 23: Representation of the structure of the algorithm.

## 4.5 Validation

A critical bug was found in the code of Guillaume Roisin [32]. Indeed, during the propagation of numerous particles, the gravitational acceleration due to Didymos of each sample was computed according to the position of the first one. As such, the validation will be realized again to assure the proper functioning of the code.

As such, a propagation of 1000 samples on 6 hour has been made, with randomly picked initial conditions. The maximum absolute error  $\epsilon_0$  is set at  $10^{-7}$ , and for *ode113*, the relative tolerance is  $10^{-16}$  and an absolute tolerance of  $10^{-17}$ . A normal distribution is used for each coordinates. The mean and the standard deviation of the distributions are shown on the table 7 :

	x [m]	y [m]	z [m]	$v_x$ [m/s]	$v_y$ [m/s]	$v_z$ [m/s]
Mean	1369	1336	-18	-0.098	-0.126	-0.07
Standard deviation	50	50	50	0.02	0.02	0.02

Table 7: Mean and standard deviation of the initial conditions.

For each propagation, the relative error is computed by looking at the norm of the difference between the result from *ode113* and the algorithm. The figures 24 and 25 shows the maximum for each sample. The mean of the maximums are shown on the table 8. The errors on the position and the velocity are mainly of the order of  $10^{-4}\%$ , but some propagation can come

up to  $10^{-3}\%$ . It is a completely reasonable error, furthermore, the validation has been made on 6h but most of the bounces do not last more than 2 hours.

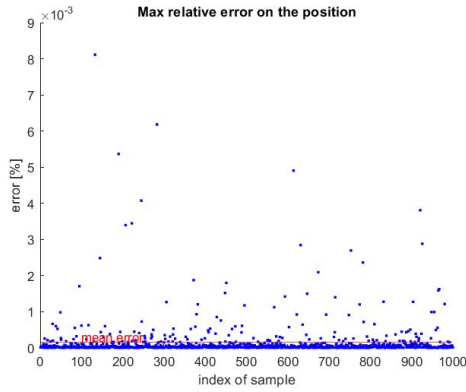


Figure 24: Maximum relative error on position on 1000 samples.

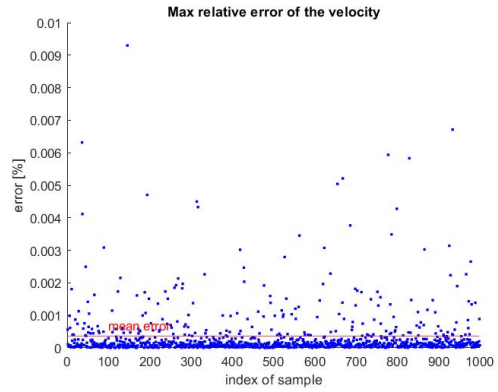


Figure 25: Maximum relative error on velocity on 1000 samples.

	Position	Velocity
Maximum of maximum of the relative error (%)	$8.1 \cdot 10^{-3}$	$9.3 \cdot 10^{-3}$
Mean of maximum of the relative error (%)	$1.5 \cdot 10^{-4}$	$3.5 \cdot 10^{-4}$

Table 8: Caption

Nonetheless, it should be interesting to look at the propagation of the error on the time. The figures 26 and 27 show the evolution the the relative error over time with 10 samples. The errors are very low during the major part of the propagation, far lower than  $10^{-4}$ . But the error suddenly increase into spikes when the time is  $> 2$  hours. As said previously, the bounce are relatively short and shouldn't be affected too much by those peaks.

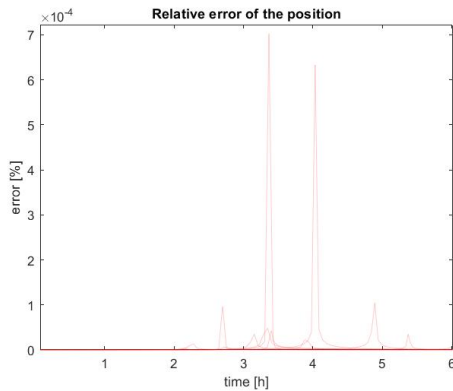


Figure 26: Relative error on position over time for 10 samples.

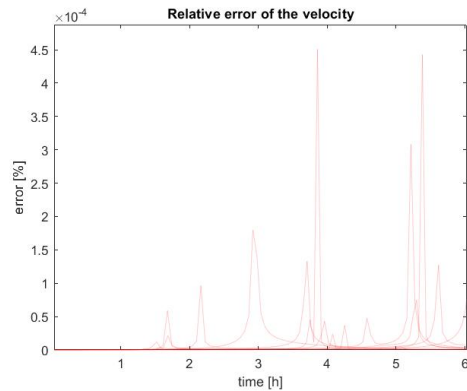


Figure 27: Relative error on velocity over time for 10 samples.



As a conclusion, the Runge-Kutta Fehlberg is a reliable method for the physical situation of the thesis. The method and the algorithm structure allows to propagate and bounce 100 satellites in 89 s, compared to 441s for the *ode113* function, so almost 5 times faster. Furthermore, the time gain becomes bigger with the increase of the number of samples. With this algorithm, a Monte-Carlo analysis could be done to estimate the behavior of Juventas when bouncing on Dimorphos.

## 5 Surface deformation

The shape model given by [11] has a major issue, more than half of its surface is approximated by a ellipsoid. Indeed, the topography comes from a scan of the surface but 100% of it could not be covered. Unfortunately, Juventas is landing on a smooth part of the surface (see figure 28). As discussed in the section 1, the surface of Dimorphos is very irregular and composed of many rocks. It is why this shape model has been transformed in order to simulate as realistic as possible a surface with rocks.

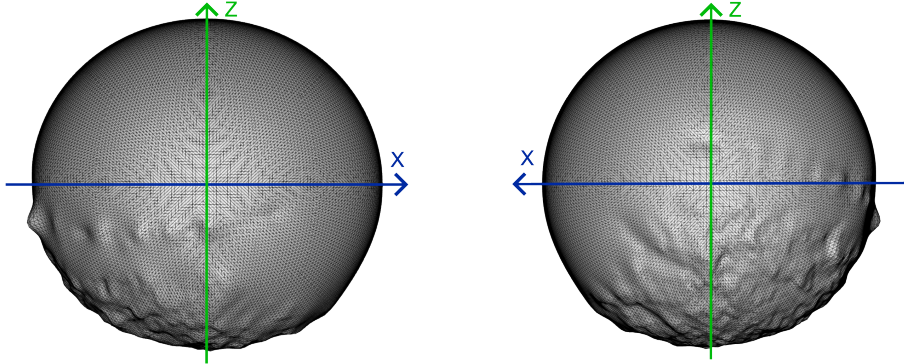


Figure 28: Side views of the shape model of Dimorphos. Left and right are the views from  $-Y$  and  $+Y$  respectively. Juventas will come from the direction  $+X$ , towards the L2 Lagrangian point. As shown, the shape on this side of Dimorphos is close to a smooth ellipsoid. Since the shape model is defined in a synodic frame, the system of axis does not move.

The transformation can be achieved by 2 ways. One way could be to add facets on the surface to emulate rocks. As such, the simulation will account new collisions and induce deviations compared to the original surface. The second way would be to directly modify the vertices of the original shape model. Since there is no way to estimate which method is the best, the both cases will be considered.

We can still notice that a way to simulate the presence of rocks on the surface would be to add randomness on the physics of bounces. Nonetheless, this method is very simple and would bring different trajectories even with the same initial conditions of position and velocity. Also, this method doesn't account for a particular topology on the surface. For example, many small rocks would have a totally different impact on than a surface with fewer rocks but with bigger shapes.

### 5.1 Rocks population

At first, adding directly generate objects on the surface will be considered. To do so, the first thing is to produce a flat surface with rocks. Then, the rocks have to be fit to the surface of Dimorphos. An algorithm has to be used to generate the shape of the rocks and arrange them

in the space. For this purpose, the ROB provided a code made by Stefaan Van wal, which successfully generate polyhedral rocks dispatched on a square plane.

### **5.1.1 Rocks placement**

The code makes first a strong assumption, the rocks have a shape near to an ellipsoid. This will drives the placement and the shape generation of the rocks. For the placement, the rocks will be placed one by one until the surface has the required density.

Initially, a length  $L$  is defined which will determine the dimensions of the square where the rocks are placed. A position and an attitude are randomly picked along with the general dimension of the first rock expressed as a major axis, a minor axis and a height. Now, an ellipsoid is defined on the plane, which represent the space that the rock will uses. To place the second rock, the same process is done but the algorithm checks if the incoming ellipsoid will overlap the first one. If it does by a too big amount, a new position and attitude are taken until a right spot is found. This process goes over and over again until the square is sufficiently full of rocks. The final result is shown on the figure 29, where each ellipsoid is a rock position.

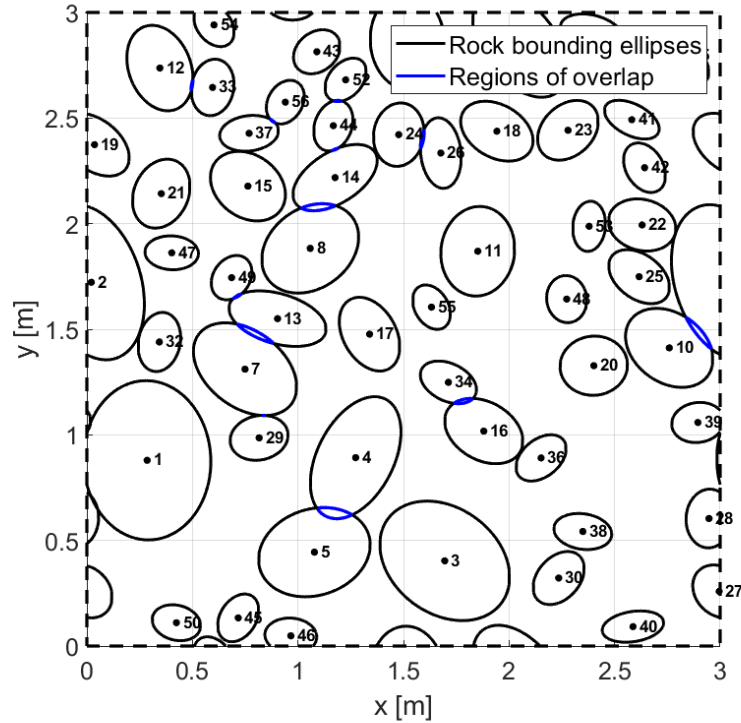


Figure 29: Graph showing the ellipsoids formed during the rock placement. Thanks to the one by one placing, the overlaps are limited.

### 5.1.2 Rock's shapes definition

Now that all rocks have a position and a general shape, a shape can be attributed to them. To do so, a polyhedron with 40 vertices is used as a reference. For an initial vertex  $\mathbf{V}$ , the new vertex is given by :

$$\mathbf{V}' = 0.5 \left( (a, b, c) \mathbf{V}^T + \sigma D \mathbf{r}_{\text{random}} \right) \quad (46)$$

where  $a, b, c$  are the major axis, the minor axis and the height of the rock respectively,  $\sigma$  the chosen uncertainty of the system,  $D$  the diameter of the overall rock diameter and  $\mathbf{r}_{\text{random}}$  a random vector of dimension 3 with coordinates picked up from a gaussian  $\mathcal{N}(0, 1)$ . Doing so transform the initial regular polyhedron to a look like rock object as shown on the figure 30.

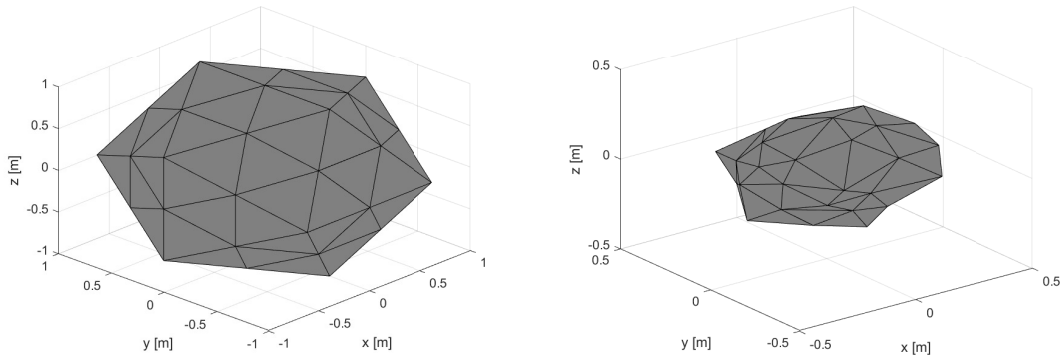


Figure 30: Example of the formation of a rock. Left : initial polyhedron. Right : final shape of the rock.

When the shape is defined, the rock is placed according to its position and with its attitude on the square. This process is repeated for each rock. When it is done, a check is done to assure every normal of the facets are oriented outwards the rocks. The result is shown on the figure 31. Usually, this shape is extended on a surface of  $3 \times 3$  the initial surface. The final object exported is a large square of rocks as shown on the figure 32, with the same pattern repeated 9 times.

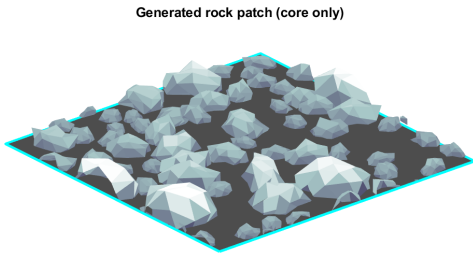


Figure 31: Final surface generated.

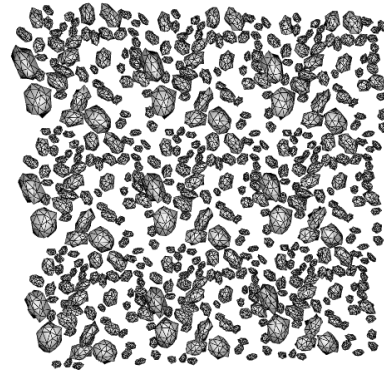


Figure 32: Extension of the rocks by  $3 \times 3$ .

### 5.1.3 Fit to the surface

Now that the rocks are generated, we have to put them on the surface of Dimorphos. Using Blender, a first flat square is created where all the rocks are placed and resized in order to fill the entire plane. Then, the surface deform modifier is used to bind the 2 objects. As such, the square will serve as a reference for all the modifications that have to be applied to the rocks. To reduce the computational time, the vertices on the other side of the reference plane are deleted since during the projection, they will be placed under the surface. It will avoid an excess use of memory and of computation time since fewer vertices induce less distance

computation.

To project the reference surface on Dimorphs, another modifier is used, shrinkwrap. Each point of the square object is projected linearly along the axis until it touch the target surface. As such, the reference surface fits to the surface of Dimorphos. The binding done just before will bring also project all the rocks on it. The figure 33 illustrates the binding of the surface and how the rocks are affected.

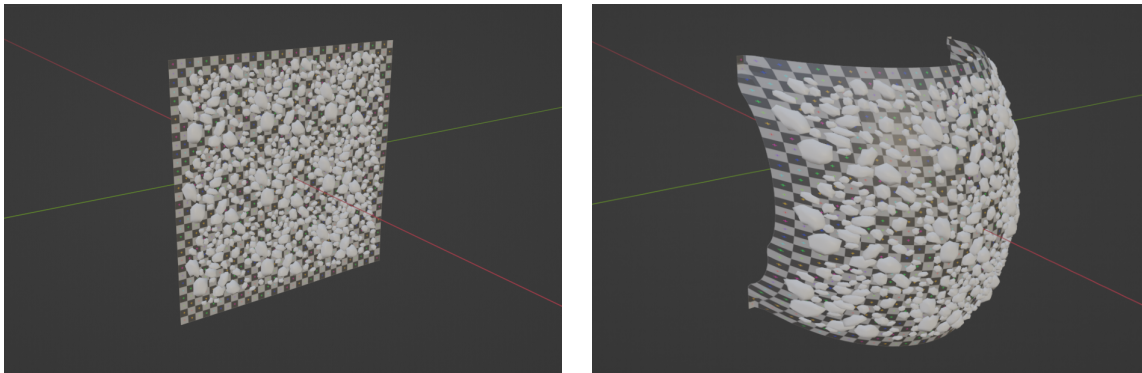


Figure 33: Image of the reference square (colored with a gray/white grid) and the rocks bind to it. On the left, the objects before the projection on Dimorphos, and on the right after the projection.

Since the propagation refers to the normals of the surface for the collision, a careful attention need to be paid to the orientation of each faces. Indeed, the algorithm uses the normals of the facets to detect the collision. A wrong normal would trigger to inaccurate bounces. As such, a check to the facet needs to be done before the exportation of the final object. Blender allows a tool to check the orientation of each facet as shown on the figure 34.

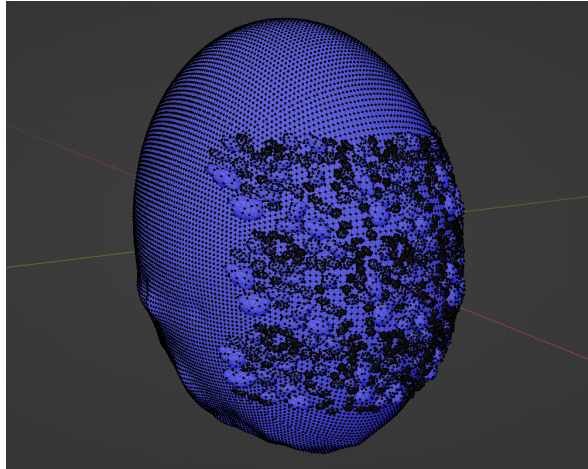


Figure 34: Image of the shape model in blender, with the filter "face orientation". The blue color shows the face where the normal is. Since the entire surface is blue, it means that the rocks have been incorporated correctly, and no corrections are needed.

Once all this process is done, the final object is obtained and can be exported. The polyhedrons of the rocks are considered by the algorithm as new facets, and the algorithm can emulate bounces at their surface.

#### 5.1.4 Parameters of rocks

Several parameters are used for the generation of rocks. The next table will show the entire values used for the shape generated for the thesis.

Smallest considered rock size	0.5 m
Largest considered rock size	2 m
Power index	-2.5
Lower cutoff diameter of model	0.192 m
C parameter	0.1/m <sup>2</sup>
Disregard rocks of which there are fewer than this limit	0.2/m <sup>2</sup>
Mean of the horizontal shape distribution	0.7 m
Standard deviation of the horizontal shape distribution	0.1 m
Minimum of the horizontal shape distribution	0.3 m
Maximum of the horizontal shape distribution	1 m
Mean of the vertical shape distribution	0.65 m
Standard deviation of the vertical shape distribution	0 m
Minimum of the vertical shape distribution	0.2 m
Maximum of the vertical shape distribution	0.9 m
Maximum overlap allowed	0.05 m
Standard deviation of each vertex of the rock	0.045 m

Table 9: List of the different parameters of the rocks.

## 5.2 Shape Model Deformation

Some issues can come from the previous method. Indeed, the shape model is no more closed since the added rocks are simply added on the surface. The increasing number of vertices has a huge impact on the computational cost. Furthermore even if rocks are added to the surface, it does not take into account for large elements of the terrain like small valleys for example. Also, it requires to use Blender instead of Matlab, which may be an issue if a Monte-Carlo analysis has to be done on the topology of the surface. It is why another method is added, which modifies directly the shape model of Dimorphos. To do so, a transformation has to be made directly to the vertex composing the surface, in a way that the shape stay closed and don't have any anomalies. Putting simply a random factor on the different vertex is not enough, it can lead to very odd surface. A commonly used method for the deformation of terrain is the Perlin noise [31], and it will be used on the entire surface of Dimorphos. Since it is a 2D noise, a method will be also used to transfer it in the 3D shape model of Dimorphos, through a mapping.

### 5.2.1 Perlin Noise

The Perlin noise is a gradient based noise, meaning that a set of randomly set of vectors are generated and will lead the general shape of the noise. The problem to solve here will be to attribute a value of change for each point in a 2D plane.

Let's imagine a finite plane containing set of  $N$  points  $\mathbf{a}_i = (\phi_i, \lambda_i) \in \mathbb{R}^2$  for  $i = 1, 2, \dots, N$  and where the noise will be applied. First, a grid is defined with  $R \times R$  squares as such it covers the entire set of points, where  $R$  will be called the resolution. Each intersection of the



grid will have a normalized vector with a random direction attributed to it. Those vectors are the gradient of the noise, and will induce the inclination of the terrain. To assure the continuity, the gradients on the top and bottom border of the grid are the same. The same thing is done to the gradients on the left and right border.

Each point  $a_i$  is contained inside a square, with 4 corners that will be noted as  $\mathbf{c}_i^{tl}, \mathbf{c}_i^{tr}, \mathbf{c}_i^{bl}$  and  $\mathbf{c}_i^{br}$  the coordinates of the top-left, top-right, bottom-left and bottom-right corner respectively. Then, the next dot products are retrieved :

$$\begin{cases} a_i^{tl} = (\mathbf{a}_i - \mathbf{c}_i^{tl}) \cdot \mathbf{g}_i^{tl} \\ a_i^{tr} = (\mathbf{a}_i - \mathbf{c}_i^{tr}) \cdot \mathbf{g}_i^{tr} \\ a_i^{bl} = (\mathbf{a}_i - \mathbf{c}_i^{bl}) \cdot \mathbf{g}_i^{bl} \\ a_i^{br} = (\mathbf{a}_i - \mathbf{c}_i^{br}) \cdot \mathbf{g}_i^{br} \end{cases} \quad (47)$$

where  $\mathbf{g}_i^{tl}, \mathbf{g}_i^{tr}, \mathbf{g}_i^{bl}$  and  $\mathbf{g}_i^{br}$  are the gradients of the top-left, top-right, bottom-left and bottom-right corner respectively. Its the dot product of the vector coming from the corner to  $\mathbf{a}_i$  and the gradient of the corner itself.

Then, a linear interpolation between the 4 dot products is used to get the final value of the noise. Nonetheless, doing so would induce a sharp surface and discontinuities derivatives between the squares of the grid. It is why a smooth function is used. Several options are available for it but in this thesis, it is defined as

$$f_s(x) = \begin{cases} 1 & \text{if } x > 1 \\ 0 & \text{if } x < -1 \\ 3x^2 - 2x^3 & \text{otherwise} \end{cases} \quad (48)$$

Combined with the interpolation, the final result of the noise  $n_i$  for  $\mathbf{a}_i$  is

$$n_i^t = a_i^{tl} + (a_i^{tr} - a_i^{tl})f_s((\mathbf{a}_i - \mathbf{c}_i^{bl})^x) \quad (49)$$

$$n_i^l = a_i^{bl} + (a_i^{br} - a_i^{bl})f_s((\mathbf{a}_i - \mathbf{c}_i^{bl})^x) \quad (50)$$

$$n_i = n_i^l + (n_i^t - n_i^l)f_s((\mathbf{a}_i - \mathbf{c}_i^{bl})^y) \quad (51)$$

where the operator  $^x$  and  $^y$  mean that either the first or the second coordinate is retrieved respectively.

### 5.2.2 Mapping

Now that the noise has been defined, let's suppose that is dispatched on a 2D map of dimension  $H \times W$ . Now, how to transpose this noise on a shape model like Dimorhpos ? Since its shape is essentially ellipsoid, we will decompose each vertex as a longitude and a latitude coordinates, that will be noted  $\lambda$  and  $\phi$  respectively. For a vertex  $\mathbf{V} = (V_x, V_y, V_z)$ , its decomposition

becomes :

$$\lambda = \begin{cases} \arccos (\sqrt{V_x^2 + V_y^2}/|\mathbf{V}|) & \text{if } V_z > 0 \\ \arccos (-\sqrt{V_x^2 + V_y^2}/|\mathbf{V}|) & \text{otherwise} \end{cases} \quad (52)$$

$$\phi = \begin{cases} \arccos (V_x/\sqrt{V_x^2 + V_y^2}) & \text{if } V_y > 0 \\ \arccos (-V_x/\sqrt{V_x^2 + V_y^2}) & \text{otherwise} \end{cases} \quad (53)$$

Now that every points are spread on a 2D plane, the Perlin noise is used to attribute a value to each point (between -1 and 1), according to their coordinates  $\lambda$  and  $\phi$ . Now that each point has its associated noise, a transposition in the 3D space is needed. As such, we define the new vertex as it follows :

$$\mathbf{V}' = (1 + 0.05 \times n)\mathbf{V} \quad (54)$$

where  $n$  is the value of the noise associated to  $\mathbf{V}$ . The value of 0.05 was chosen accordingly to the irregularities already present on the surface. It limits the deformation of the original vertex up to 1/20 of their norm.

The figure 35 illustrate all the process and shows the final result. An important detail is the deformation on the poles of the ellipsoid, where the shape model seems to be crumpled. It is due to the longitude and latitude coordinates that are less denser near the poles. Those effects can be explained thanks to the Gauss's Theorema Egregium [38]. A consequence of this theorem is that no isometries can exist between an ellipsoid and a plane. So whatever the method of mapping chosen, it will always contain some inaccuracies due to the transformation. Nonetheless, with the actual choice of coordinates, the distortions are mainly affecting the poles, which are relatively far from the landing site. As such, it is considered as a minor issue.

### 5.2.3 Resolution

The main parameter for the noise generation is the resolution  $R$ , which determines number of squares in the grid. More squares means more gradients and so, more irregularities on the noise. A set of different shapes according to the resolution is shown on the figure 36.

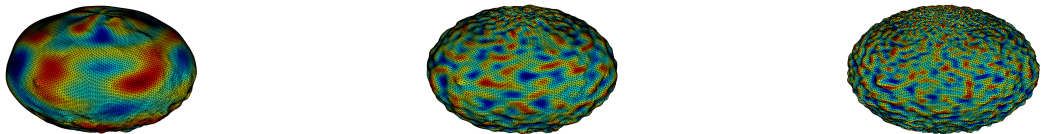


Figure 36: 3 shape models with Perlin noise, but with different parameters  $R$ . From left to right,  $R = 10, 30, 50$ .

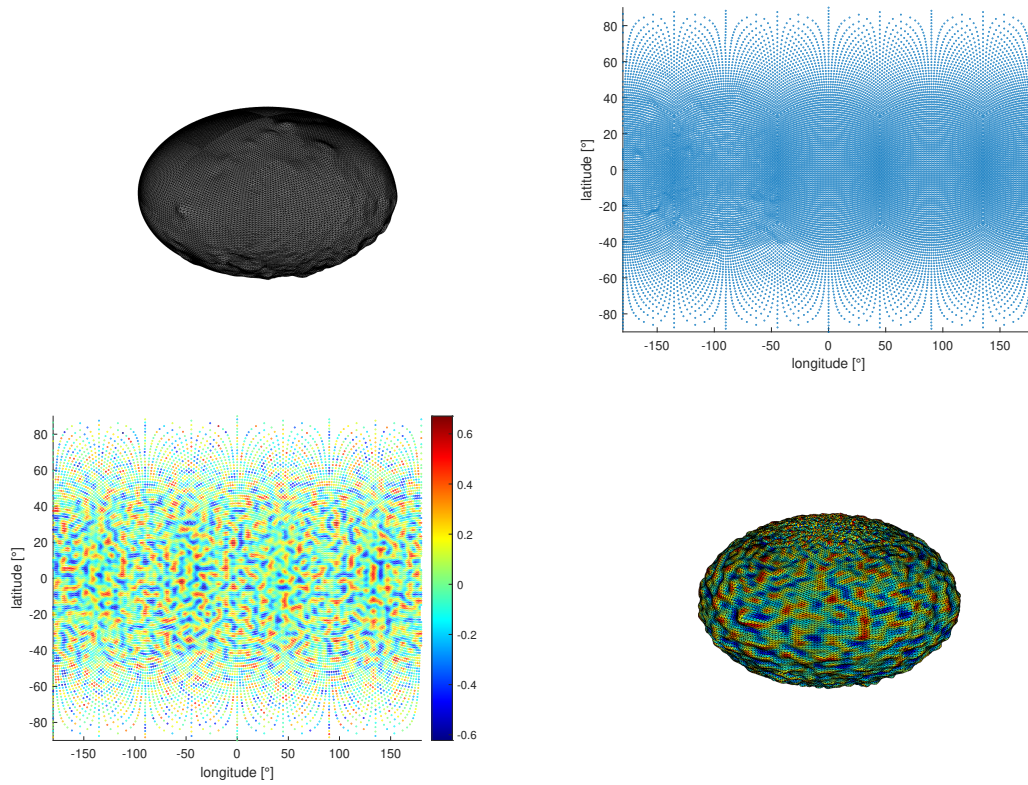


Figure 35: The 4 steps in order to produce a noisy shape model. Top-left : Original shape model. Top-right : Decomposition in longitude and latitude of the vertex. Bottom-left : Longitude and latitude coordinates with the noise associated to it. The values of the noise are dimensionless. Bottom-right : Final shape model with the noise.

## 6 Monte-Carlo Analysis

To account for the uncertainties of the physical system studied, a Monte-Carlo analysis is performed in order to consider a large range of variables for this work. First, the preliminaries of the analysis are set. Then an analysis of the main features like the position and the landing velocity is made. A careful attention is then delivered to the coefficient of restitution. The chapter finish on a discussion about the importance of solar panels, and the study of a case without them.

### 6.1 Preliminaries

Before making any analysis, the uncertainties for Juventas need to be set up, and determine how many samples should be run. Due to the high computational cost, the number of samples need to be as low as possible without sacrificing too much the quality of the Monte-Carlo data set. Each of these process will be explained.

#### 6.1.1 Uncertainties

For the choice of the position and the velocities, a normal distribution is chosen to generate the different initial conditions, as shown on the table 10. Thanks to the analysis of GMV, the trajectory of Juventas and the uncertainties associated are known. The mean position and velocity are the values just before the braking maneuver, since it is the only maneuver included in the code. Also, our propagator is very simple and taking the latest values before the braking maneuver as much as possible the errors brought by ignoring some perturbations (like the solar radiation pressure for example).

Note that no uncertainties are applied to the maneuver. Indeed, they are already present on the position and the velocity, adding another variable on the maneuver was considered superfluous.

	x [m]	y [m]	z [m]	$v_x$ [m/s]	$v_y$ [m/s]	$v_z$ [m/s]
Mean	1358	-28	-22	0.061	-0.04	-0.022
Standard deviation	11.54	9.04	9.25	0.002	0.001	0.002

Table 10: Mean and standard deviation of the initial conditions on the position and the velocity.

Concerning the attitude of Juventas, the normal distribution will also be used. Nonetheless, the attitude will be expressed as a quaternion and each term (real and imaginary) are chosen through a Gaussian distribution. Juventas is supposed to land on the face equipped with the camera, so on the +Z axis according to the figure 17. To reverse Juventas, the mean attitude is set to  $q = \frac{\sqrt{2}}{2} + \frac{\sqrt{2}}{2}i$  corresponding to a rotation of 180° along the Y axis so the CubeSat has the good orientation (see the appendix 8.4 for information about quaternion) The mean of the rotation vector  $\omega$  is set to 0 since Juventas should be stable during the landing. The standard deviation for each variable are unknown and so, a value of 0.01 has been chosen for

each dimension. The values for the mean and the standard deviation are shown on the table 11.

	q ( <i>real</i> )	q (i)	q (j)	q (k)	$\omega_x$ [rad/s]	$\omega_y$ [rad/s]	$\omega_z$ [rad/s]
Mean	0.7071	-0.7071	0	0	0	0	0
Standard deviation	0.01	0.01	0.01	0.01	0.01	0.01	0.01

Table 11: Mean and standard deviation of the initial attitude of Juventas.

As explained on the section 3.3.2, the only surface properties that will be varied are the static coefficient of friction and the damping coefficient. The conditions of Dimorphos are unknown, it is why an uniform distribution will be used for the 2 parameters so a large range of values are considered. The minimum and maximum are chosen accordingly to measurements of other asteroids (see section 3.3.2 for detailed explanation). The values for the mean and the standard deviation are shown on the table 12.

Variable	$\mu_s$	$\Gamma$ [kg/s]
Min	0.3	40
Max	0.8	4000

Table 12: Range of the different variables for the surface properties.

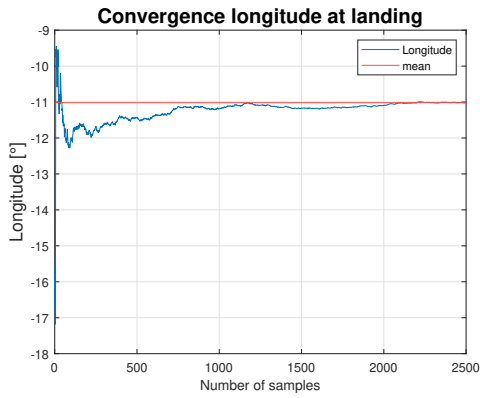
### 6.1.2 Convergence

Every Monte-Carlo analysis needs a convergence analysis to estimate the number of samples to run during a simulation. Since the simulations can last several hours, a limit needs to be set in order to perform several analysis, especially for the section 7 that requires a lot of simulations.

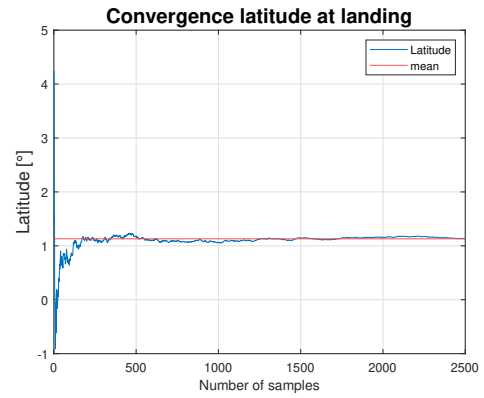
Here are the parameters considered for the analysis :

- Longitude at landing (at the first impact)
- Latitude at landing
- Longitude at rest
- Latitude at rest
- Duration of bouncing
- Number of bounces
- Landing velocity

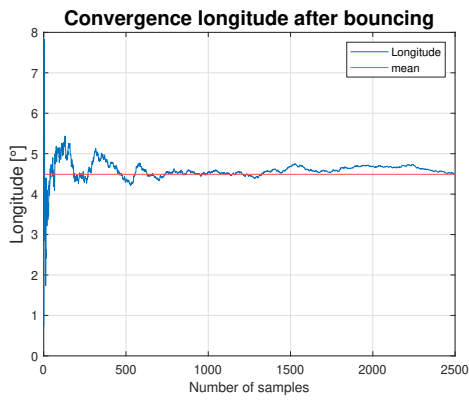
A test is performed on 2500 samples and lasted 16h, and the means of every parameter are shown on the figure 37. The convergence is obtained around 1000 samples for each parameter.



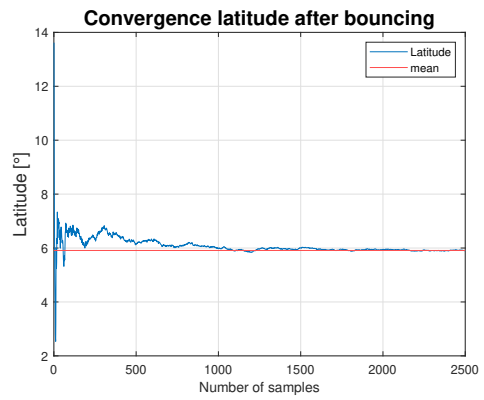
(a) Mean longitude at impact.



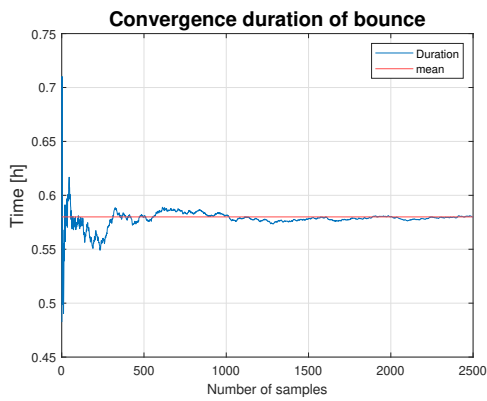
(b) Mean latitude at impact.



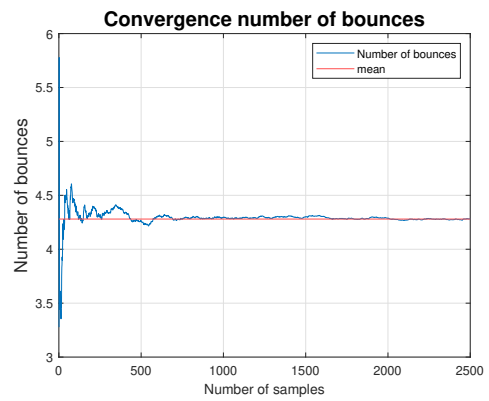
(c) Mean longitude at rest.



(d) Mean latitude at rest.



(e) Mean duration of bounce.



(f) Mean number of bounces.

Figure 37: Convergence for 2500 samples.

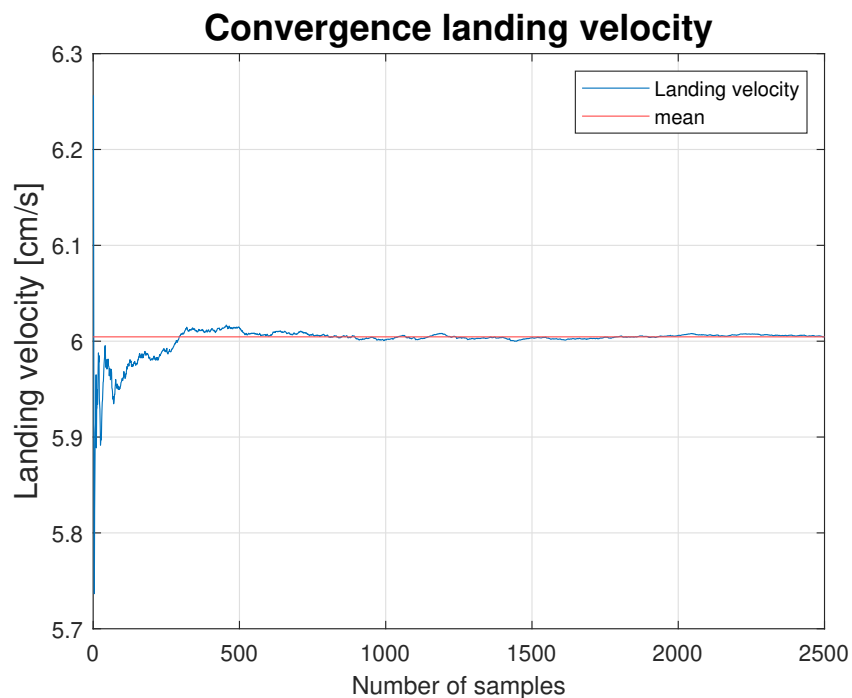


Figure 38: Mean of the landing velocity for 2500 samples.

It is a low amount for a Monte-Carlo analysis but considering the computational time for the simulation (at least 6h for 1000 samples), the minimum amount has to be chosen in order to perform enough tests on different surfaces. Nonetheless, we can argue that the most important parameters is the landing velocity on the figure 38, since it will lead the entire bounce on the surface. And we see clearly that it converges well before 1000 samples.

## 6.2 Landing and bouncing trajectories

The set of data is obtained from 1000 samples performed on the surface of Dimorphos, some trajectories are shown on the figure 39 with the shape model. The trajectory of Juventas is expected from a bouncing trajectory. The collision detection appears to be correct, no distant bounces occur like in the figure 12. Nonetheless, the bounces can be relatively random, especially on the last ones where the speed is lower. We are very far from "perfect" trajectories like in the previous thesis [32], and the behavior of the satellite is clearly more complex.

It is hard to check the bounces inside Matlab for each sample. Instead, the first bounce of a randomly taken sample will be overlooked on the figure 42. The attitude of the spacecraft is already tilted, essentially because the spacecraft rotated after the braking maneuver during a long period of time. The CubeSat approaches the surface with a velocity of 6.5 cm/s. During the impact, the solar panels bend and absorb some of the energy of the impact. After the bounce, the satellite continues its trajectory to the left. The initial rotation speed of 0.01 rad/s becomes 0.08 rad/s, showing that a part of the energy is also converted in rotational energy. This kind of behavior is expected from this new model.

The landing trajectories seem to change drastically above Dimorphos. It is simply a combination of the braking maneuver and the choose of frame of reference. Since we are in a rotating frame, virtual forces act on Juventas along with the acceleration due to the braking maneuver. It leads to this kind of curved trajectories.

The landing position and resting position can be expressed in term of latitude and longitude since the surface of Dimorphos is near to an ellipsoid. As such, the distributions are shown on the figure 41. The mean and the standard deviations of each distributions are shown on the table 13. Note that the latitude and longitude are set such as the axis +X is at 0° for both coordinates, pointing at the L2 point.

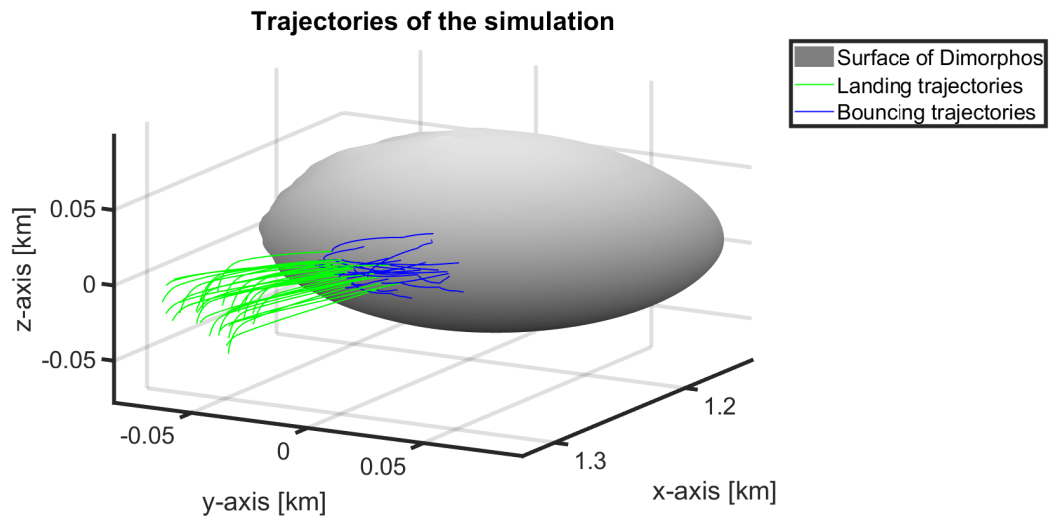
	lat landing [°]	long landing [°]	lat resting [°]	long resting [°]
Mean	1.06	-11.18	5.95	4.45
Standard deviation	3.35	5.98	7.63	12.20
	Duration [h]	Number of bounces	Landing velocity [cm/s]	Incident angle [°]
Mean	0.60	4.24	6.00	60.90
Standard deviation	0.30	2.08	0.28	5.55

Table 13: Mean and standard deviation for different parameters.

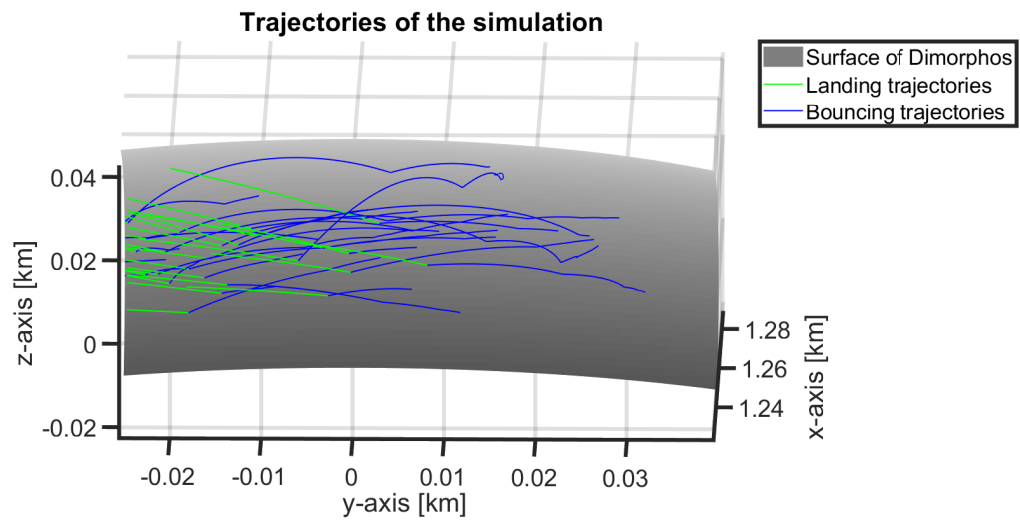
A first interesting result is the incident angle. Indeed, the mean angle is 60.90° with a standard deviation of 5.55°, meaning that the spacecraft almost never land vertically to the ground.

For the latitude and the longitude at landing, the distribution is close to a normal distribution if we look at the figures 40a and 40b, which is expected since the choice for initial conditions are based on Gaussian distributions. The estimated landing position is then (1.06°, -11.18°), with a relatively large uncertainty. Indeed, the figure 41a shows different error ellipses with different intervals of confidence. The 95% ellipse is larger than 20° on longitude, meaning the





(a) General view of the trajectories.



(b) View near to the surface.

Figure 39: Samples of 30 trajectories.

dispersion is very high along the geographical parallel.

Nonetheless, the dispersion is even higher for the position after the bouncing. Indeed, the standard deviation is more than doubled for each coordinate. It is impressive, since the previous work [32] had a constant standard deviation between the impact and the position at rest. It shows that considering the rotations and the 3D shape of Juventas, along with the new surface properties, adds more randomness to the propagation.

The next part of the thesis will refer to the cardinal points in order to facilitate a simpler discussion of trajectory directions. So the east and west are the directions towards positive and negative longitude respectively. The mean position at rest is  $(5.95^\circ, 4.45^\circ)$ , so there is a clear shift towards the east between the landing and the bounce. It is coherent if we look at the figure 39, where the trajectories are oblique towards the east. So it is expected to have a higher longitude after the bouncing. As shown on the figure 41f, the incident angle is relatively high, and so this behavior is recurrent.

The figure 41c shows a trend. The impact velocity is higher on the east than on the west. It is mainly due to the incoming trajectory of Juventas. The faster samples tend to go further and so, land on the eastern part of the landing site.

On the entire data set of 1000 samples, none of them has ever bounced off the surface of Dimorphos, leading to a success rate of the mission of 100%. Nonetheless, the data set is relatively small and maybe some particular conditions for the bouncing to occur has been missed. Also, it will be more discussed on the next subsection, but the coefficient of restitution is lower compared to the first theoretic estimations.

We can note that the landing velocity computed by GMV is 5.98 cm/s, and here the mean value is 6.00 cm/s. It is a comforting result for the validation of the model.

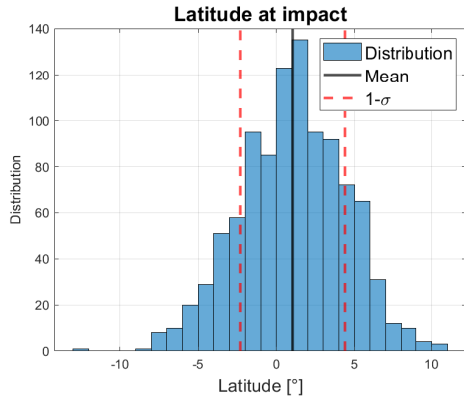
### 6.3 Coefficient of restitution

It is common in bounce modeling to introduce a coefficient of restitution. Here, simply taking the ratio between incoming and outgoing velocity would not account for the rotation of Juventas. As such, the energetic coefficient of restitution is instead considered as it follows :

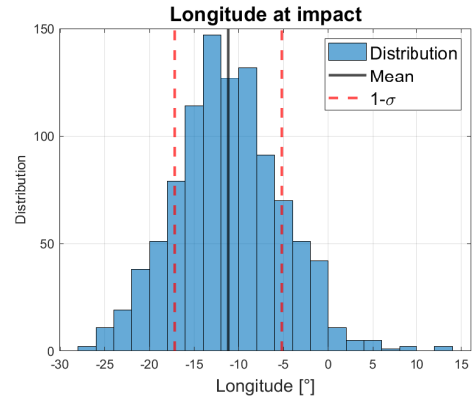
$$\mathbf{Coeff} = \frac{mv_i^2 + \boldsymbol{\omega}_i \cdot \mathbf{I}\boldsymbol{\omega}_i}{mv_f^2 + \boldsymbol{\omega}_f \cdot \mathbf{I}\boldsymbol{\omega}_f}$$

where  $v$  and  $\boldsymbol{\omega}$  are the norm of the velocity and the rotational vector respectively, the indices  $i$  and  $f$  indicates if they are before or after the bounce respectively.  $m$  and  $I$  are the mass and the inertia matrix taken from mechanical report of Juventas [7].

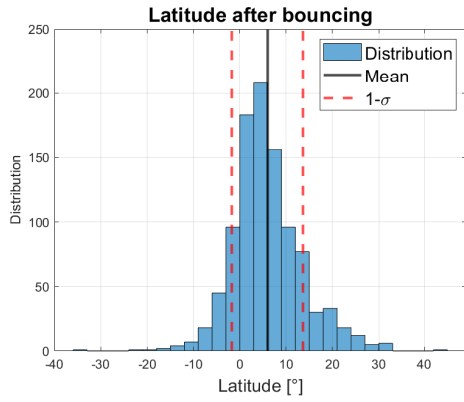
The coefficient of restitution should be connected with the damping coefficient of the surface. Nonetheless, it is not the case on the figure 43. Indeed, the initial estimations (see appendix 8.4) overestimate the actual bouncing of the samples. The coefficient tend to be



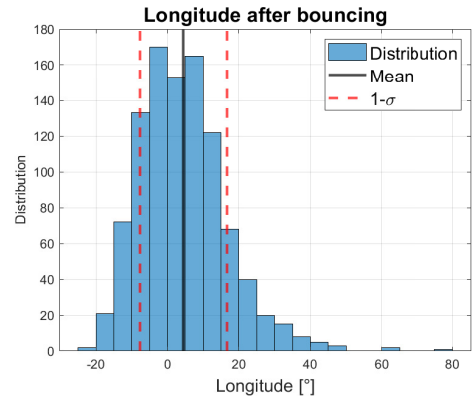
(a) Latitude at the first impact.



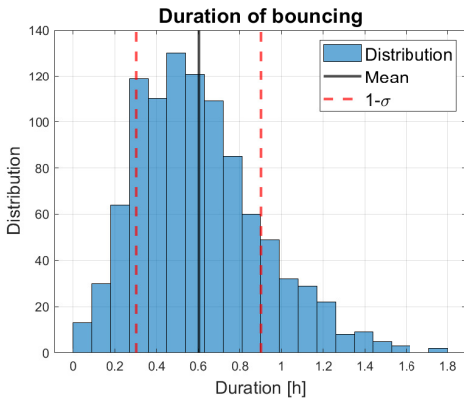
(b) Longitude at the first impact.



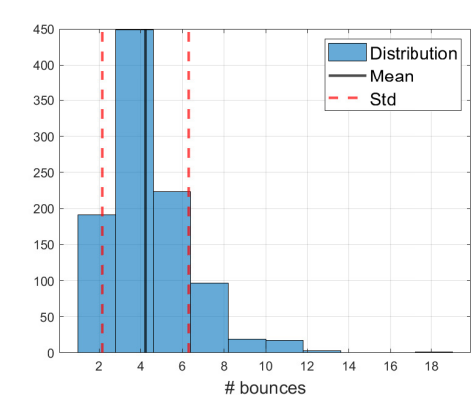
(c) Latitude after the bouncing.



(d) Longitude after the bouncing.

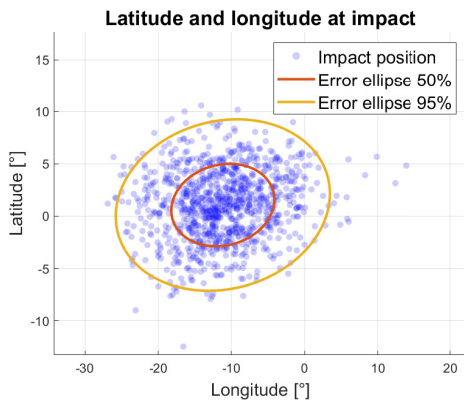


(e) Duration of the entire bounce.

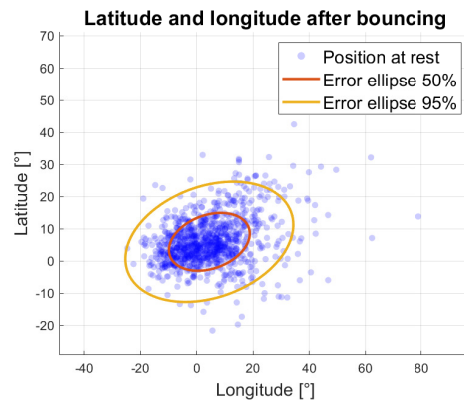


(f) Number of bounces.

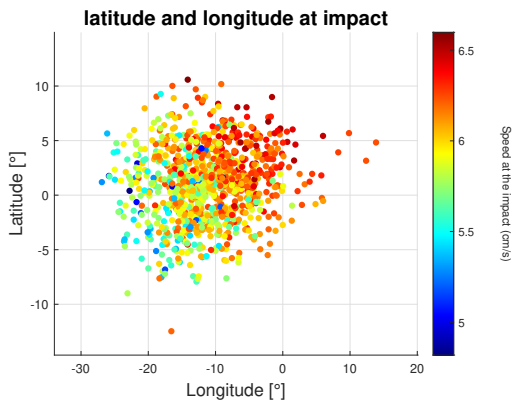
Figure 40: Histograms of different parameters for 1000 samples.



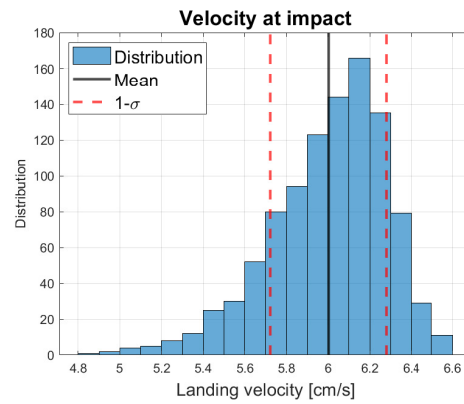
(a) Latitude and longitude of the different samples at the first impact.



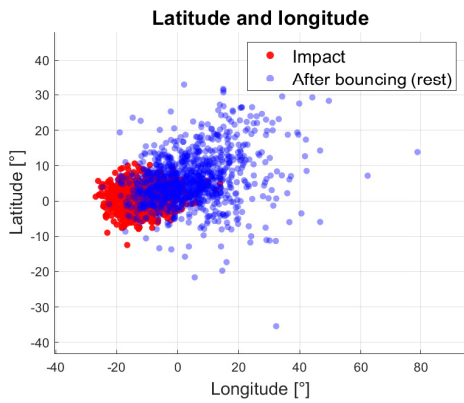
(b) Latitude and longitude of the different samples at rest.



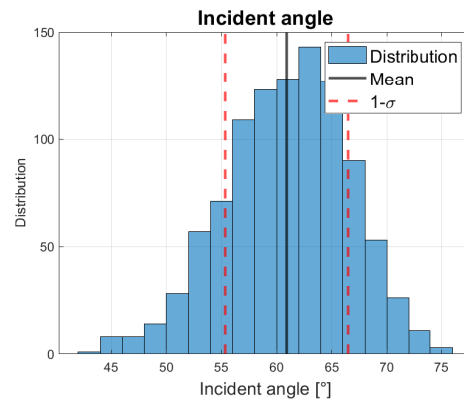
(c) Latitude and longitude at impact with the impact velocity.



(d) Landing velocity distribution.



(e) Latitude and longitude at impact and at rest.



(f) Distribution of the incident angle.

Figure 41: Graphs of position at impact and landing, along with information about the landing velocity or the incident angle.

higher when the damping coefficient is lower, which was expected. But the vertical spread of the values is surprising. Since the solar panels were modelled as damped spring, the CubeSat can absorb and dissipate the through shocks.

In order to see which parameters can affect the coefficient, the figure 44 shows the relation between the coefficient of restitution and different other parameters. There are no clear relation on the different graphs. Nonetheless, the coefficient of restitution seems to reduce the incident angle. It seems the CubeSat is more likely to dissipate energy through friction with high angles.

The coefficient of restitution seems to have no effect on the contact time. Still, when the contact time is superior to 0.04 second, no samples could have a coefficient superior to 0.4. It seems that when contact time is high, the damping is very effective.

The graphs with the max acceleration and the initial energy are both clouds of dots, but no trend can be seen.

Different parameters are varying with the coefficient of restitution, as shown on the figure 45. Indeed, the duration of bounce and the max height are increasing with it, which is expected. On the other hand, the number of bounces seems unaffected.

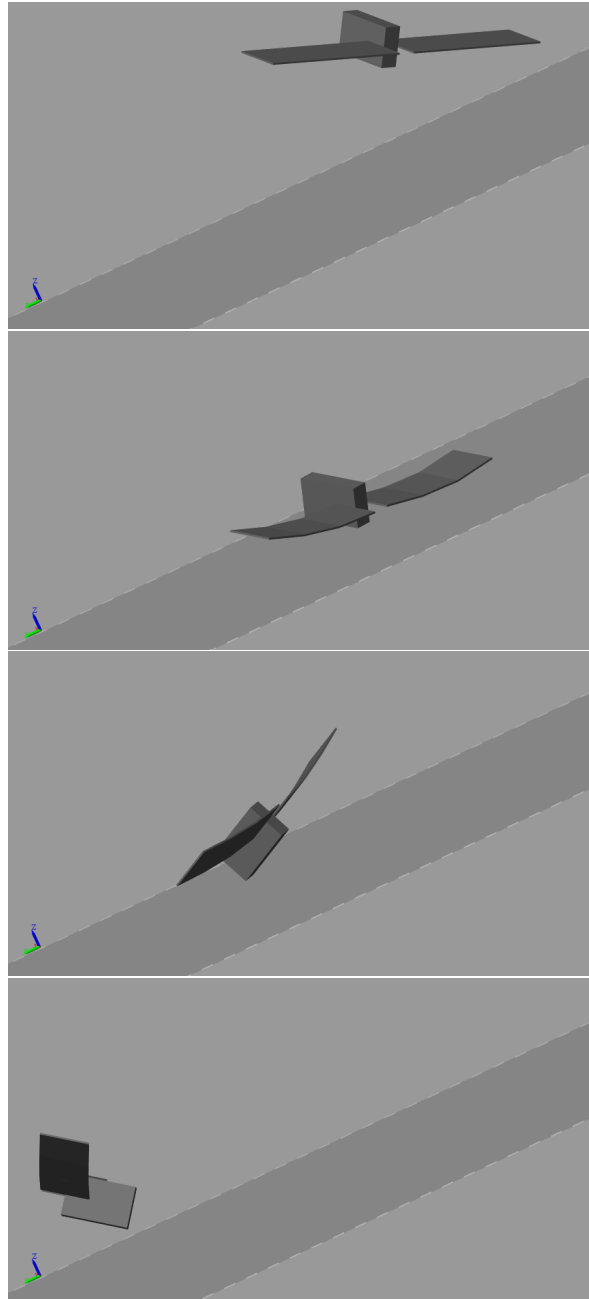


Figure 42: Different frames from the first bounce of Juventas. The first image from the top is taken before the contact with the ground. The second during the impact and the third just after. The bending of the solar panels is clearly seen on these 2 figures. The last one is taken before the simulation stops. The solar panels are still bent and continues to oscillate.

### Coefficient of restitution vs Damping coefficient

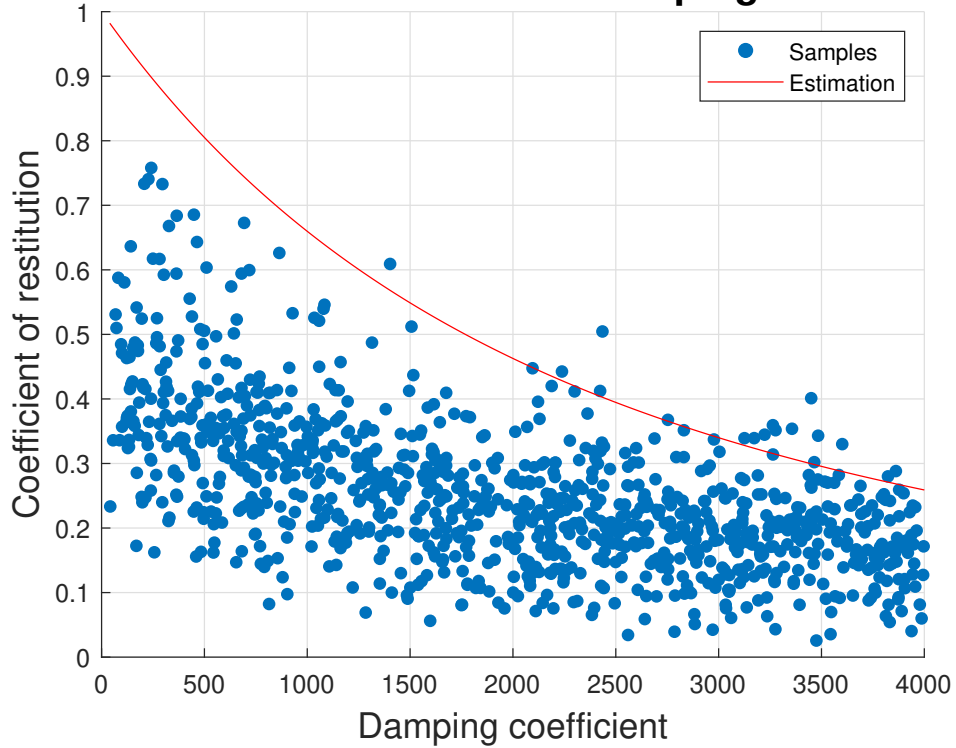
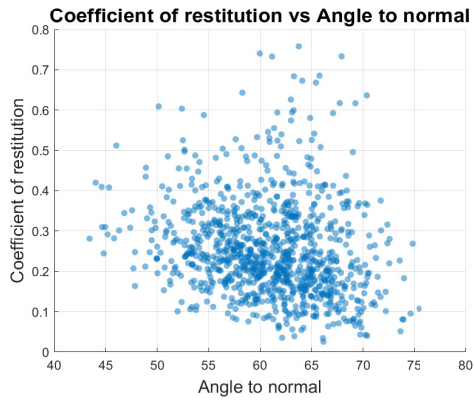
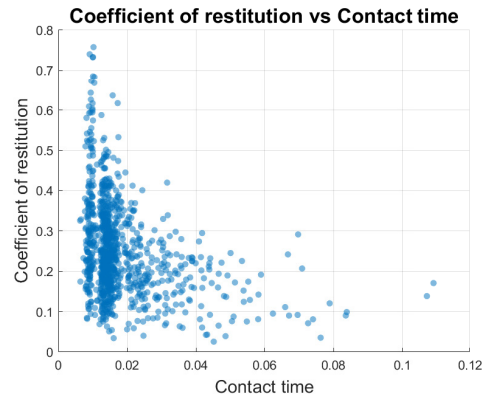


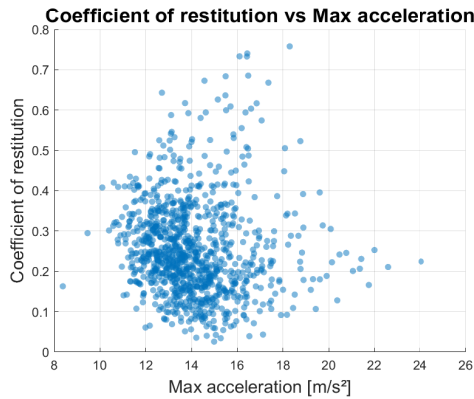
Figure 43: Computed coefficient of restitution on the 1st bounce with the damping coefficient of each sample. The estimation is computed in the appendix 8.4.



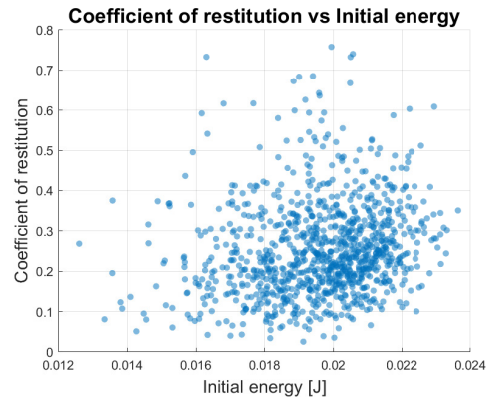
(a) Coefficient of restitution along the incident angle.



(b) Coefficient of restitution along the contact time with the ground.



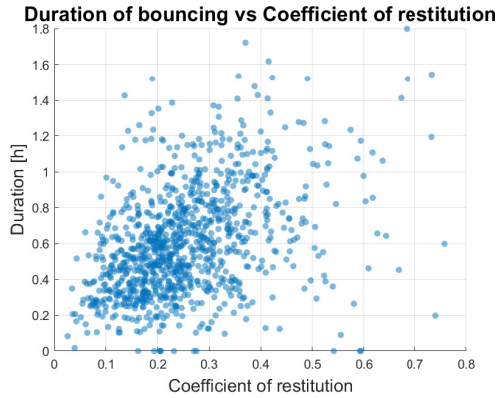
(c) Coefficient of restitution along the max acceleration experienced during the bounce.



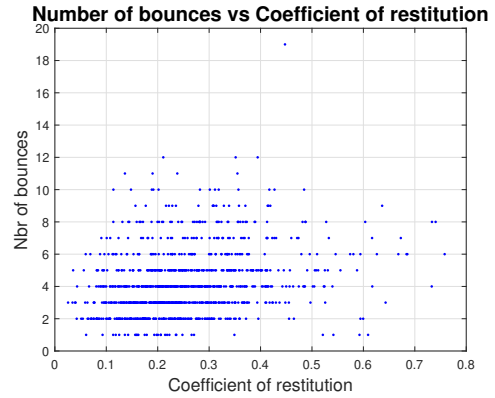
(d) Coefficient of restitution along initial energy before the bounce.

Figure 44: Coefficient of restitution along other parameters during the bounce on the smooth shape model.

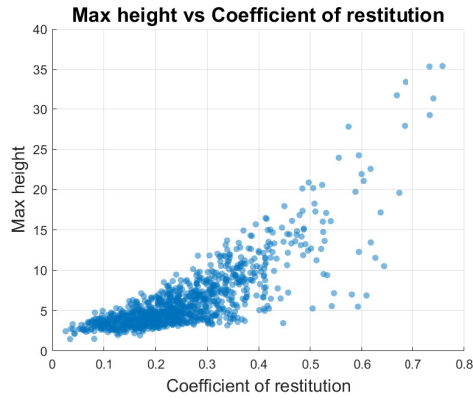




(a) Duration of bouncing along the coefficient of restitution.



(b) Number of bounces along the coefficient of restitution.



(c) Max height along the coefficient of restitution.

Figure 45: Different parameters along the coefficient of restitution computed on the smooth shape model. The height is evaluated on an ellipsoid of reference of  $170 \times 190 \times 110m$ , which is a good approximation of the surface of Dimorphos.

## 6.4 Solar panels

During the landing, the solar panels, especially the hinges, are exposed to external forces and deformations. Each joint cannot bend too hard, otherwise permanent deformation could be done to hinges and it could affect the efficiency of the solar panels. The manufacturer of the joints indicate a max torque angle up to  $294^\circ$  [1]. Nonetheless, it does not show when inelastic deformation will occur. As such, an arbitrary limit is set  $90^\circ$  as the limit for inelastic deformations.

The figure 47 shows the distribution of the maximum deflection angle for each joint. For the disposition of each joint in 3D, see figure 46. The mean of each joint never surpass  $20^\circ$ , and even extreme values never surpass  $50^\circ$  on each histogram, which is well below the limit for non-elastic deformation. As such, the landing of Juventas can be considered as safe for the solar panels according to this model.

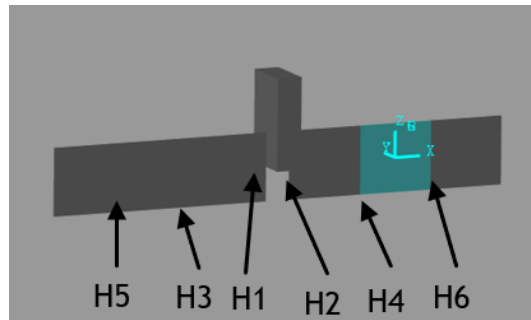


Figure 46: Scheme showing the disposition of each joint.

To understand the evolution of the deflection angle, the figure 48 shows the evolution of the deflection angle for each joint on the first bounce of a randomly picked sample. Before hitting the surface, the spacecraft has its solar panels at  $0$  rad for each joint, as expected. During the contact, each joint is bent on the same direction. But after leaving the surface, continues to oscillate. It shows clearly that a part from the incoming energy of the spacecraft is deviated through the solar panels.

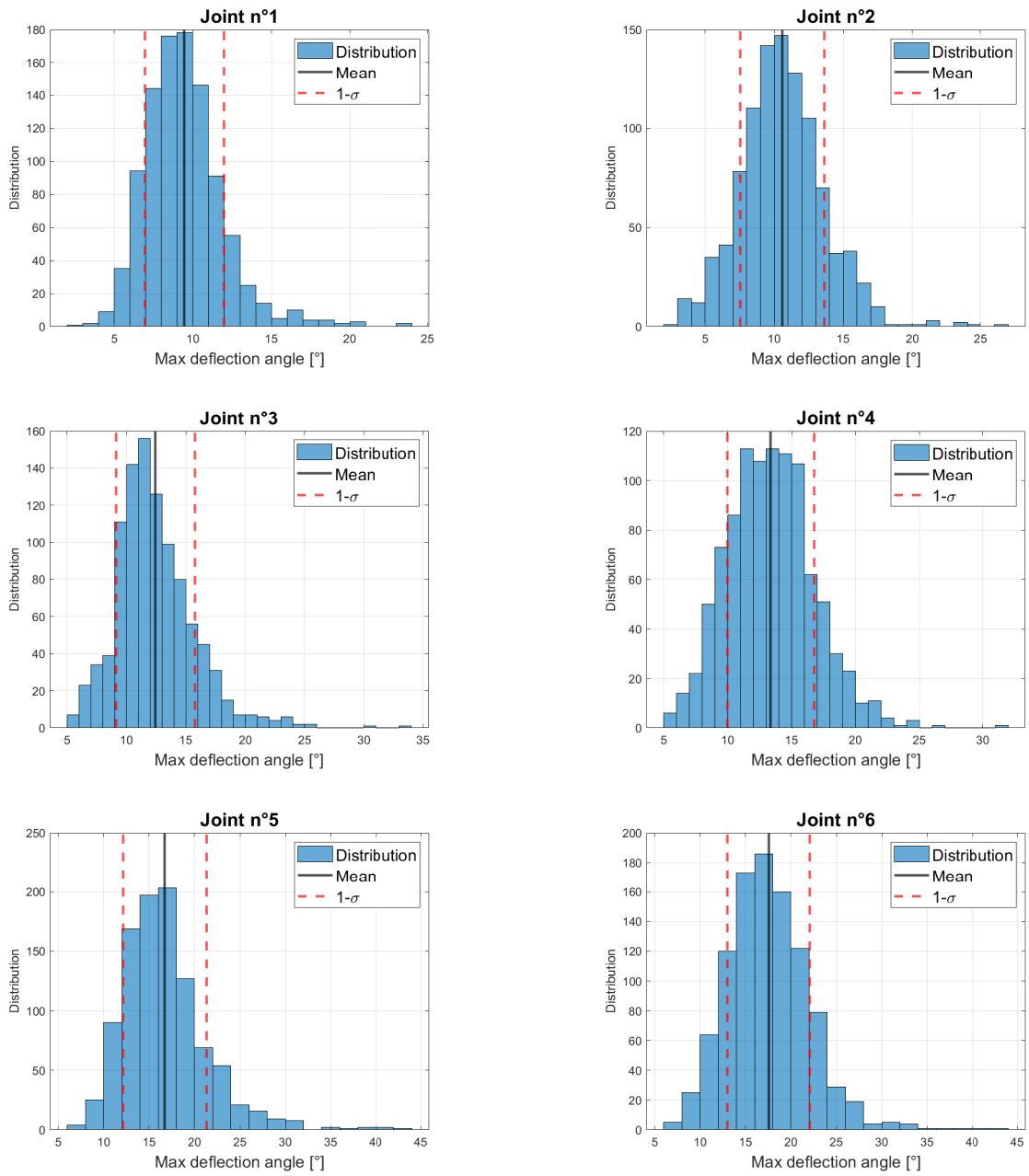


Figure 47: Distribution of the deflection angle on all the joint of the solar panels.

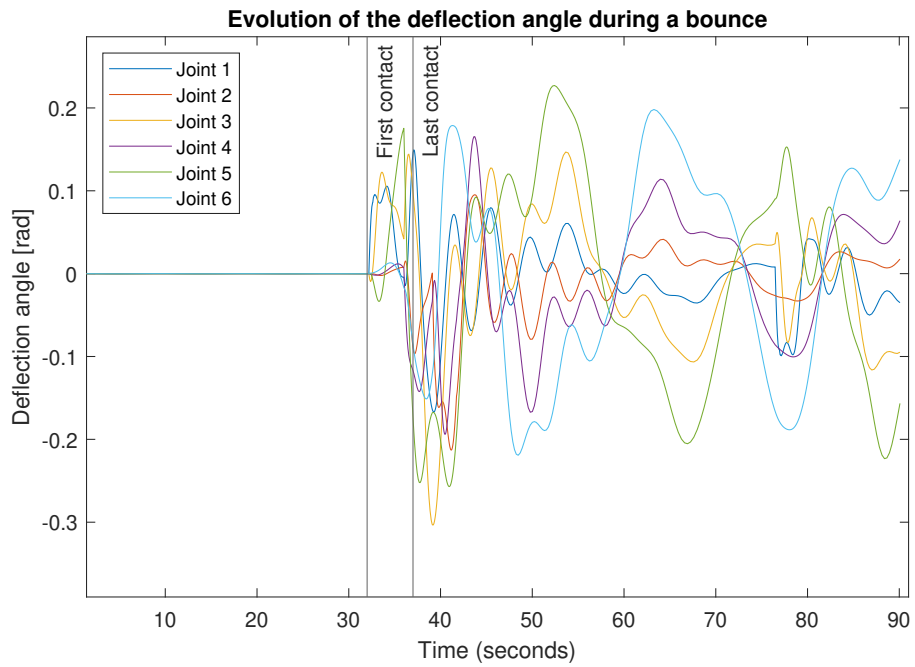


Figure 48: This figure shows the evolution of the deflection angle for each joint during the first bounce of a randomly picked sample. 2 lines indicate when the satellite hits the ground and when it leaves it.

## 6.5 Retraction of solar panels

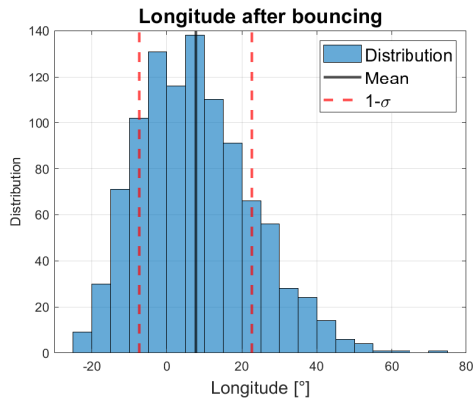
An interesting study would be to ignore the solar panels, and only consider the main body of Juventas. To do so, a new matrix of inertia is taken from [7], with the solar panels retracted. To make a comparative study, the initial conditions and the seed for the random number generator are the same (see tables 10, 11 and 12). The table 14 shows the new results.

	lat landing [°]	long landing [°]	lat resting [°]	long resting [°]
Mean	1.06	-11.18	6.93	7.69
Standard deviation	3.35	5.98	10.08	15.00
	Duration [h]	Number of bounces	Landing velocity [cm/s]	Incident angle [°]
Mean	0.55	8.23	6.00	60.90
Standard deviation	0.37	4.51	0.28	5.55

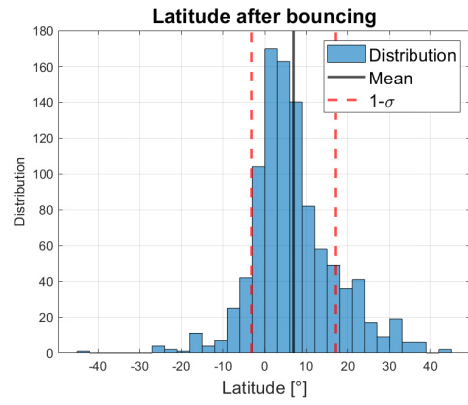
Table 14: Mean and standard deviation for different parameters without solar panels.

As expected, the values for the landing do not change since the initial conditions are strictly the same. On the other hand, the result for the bounce are totally different.

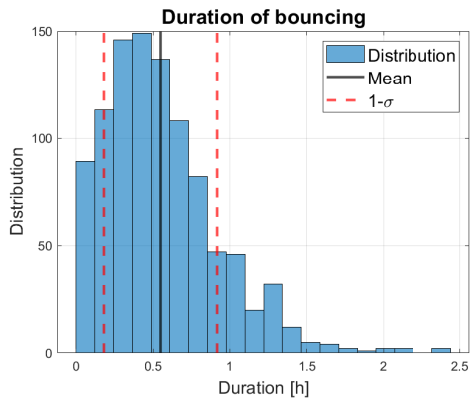
A small shift can be seen on the mean, from the coordinates (4.45°,5.95°) to (7.69°,6.93°). The bounces propagate further without the solar panels, reinforcing the idea that they dissipate energy through oscillations. But the change is also present for the dispersion, since the standard deviation of both coordinates increase. Also, the number of bounces increases. It can be assumed that the solar panels can act as shock absorber during the last bounces. Nonetheless, an unexpected result is the duration of bounce. Instead of increasing, it slightly decreases. Even if the difference is small, only 0.05 h, the absence of solar panels as damper should allow more energy for the aftershock velocity. A histogram for those parameters are available on the figure 49.



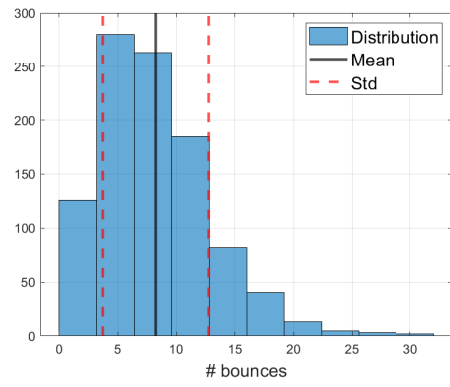
(a) Longitude at rest distribution.



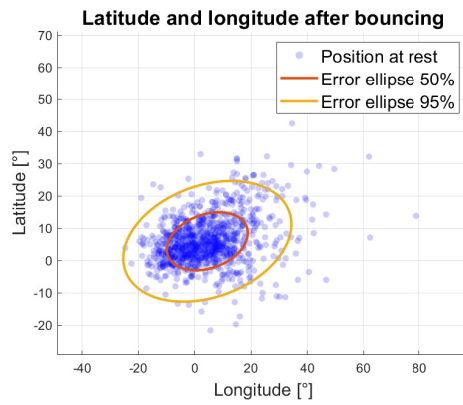
(b) Latitude at rest distribution.



(c) Duration of bounce distribution.



(d) Number of bounces distribution.



(e) Latitude and longitude at rest.

Figure 49: Graphs of different parameters from a simulation without solar panels.

## 7 Surface variation

This chapter undertakes an examination of the effects of surface deformation. It delves into the overarching outcomes across various surfaces, thoroughly investigating and analyzing their implications. The two methods described on the chapter 5 are used and analyzed.

### 7.1 Perlin noise

The programmed Perlin noise allows to perform easily simulations on different surface. As such, 5 surface are tested with 1000 samples and progressive factor R. The initial conditions are the same that on the table 10 and 11. The surface properties are set to  $\mu_s = 0.5$  and  $\Gamma = 1000$  kg/s. In order to have the same generated conditions, each simulation have the same seed for the random number generator. As such, no study will be done on the landing since it is the same trajectories for each simulation.

The positions after bouncing for each simulation are shown on the figure 50. It is clear that for lower values of R, the ellipses of error are elongated, similarly to the simulation in the previous section. On the other hand, the dispersion increases drastically for  $R > 30$ . The uncertainty becomes bigger on the latitude, which leads to more circular ellipses of error.

Different parameters are shown on the figure 52. First, the area of the error ellipses gives a good indication of the dispersion. The first shows a strong increase when R reaches 30, but then no further change are seen. On the other hand, the number of bounces and the duration bouncing increase more linearly, showing the clear impact of the surface on the different parameters.

### 7.2 Rock population

The same conditions for the analysis defined on the previous subsection are used. Nonetheless, the method to form the surface here is by using the code from Stefaan Van wal and integrate it through blender. Due to the difficulty to form the shape model and due to the huge increase of the computational cost by adding vertex, the simulation was done on only one surface.

According to the previous results with the Perlin noise, an increase in the duration of bouncing (mean = 0.82 h) can be observed, especially on the number of bounces (mean = 9.46) which is the highest of all the noisy terrain. Nonetheless, the area of the error ellipse at 50% is relatively low compared to other tests (area = 407), meaning the dispersion seems to not be affected by the rocks adding.

Adding those individual rocks on the surface privilege little bounces, which leads to this high increase in number of bounces. Nonetheless the dispersion does not seem to be very affected.

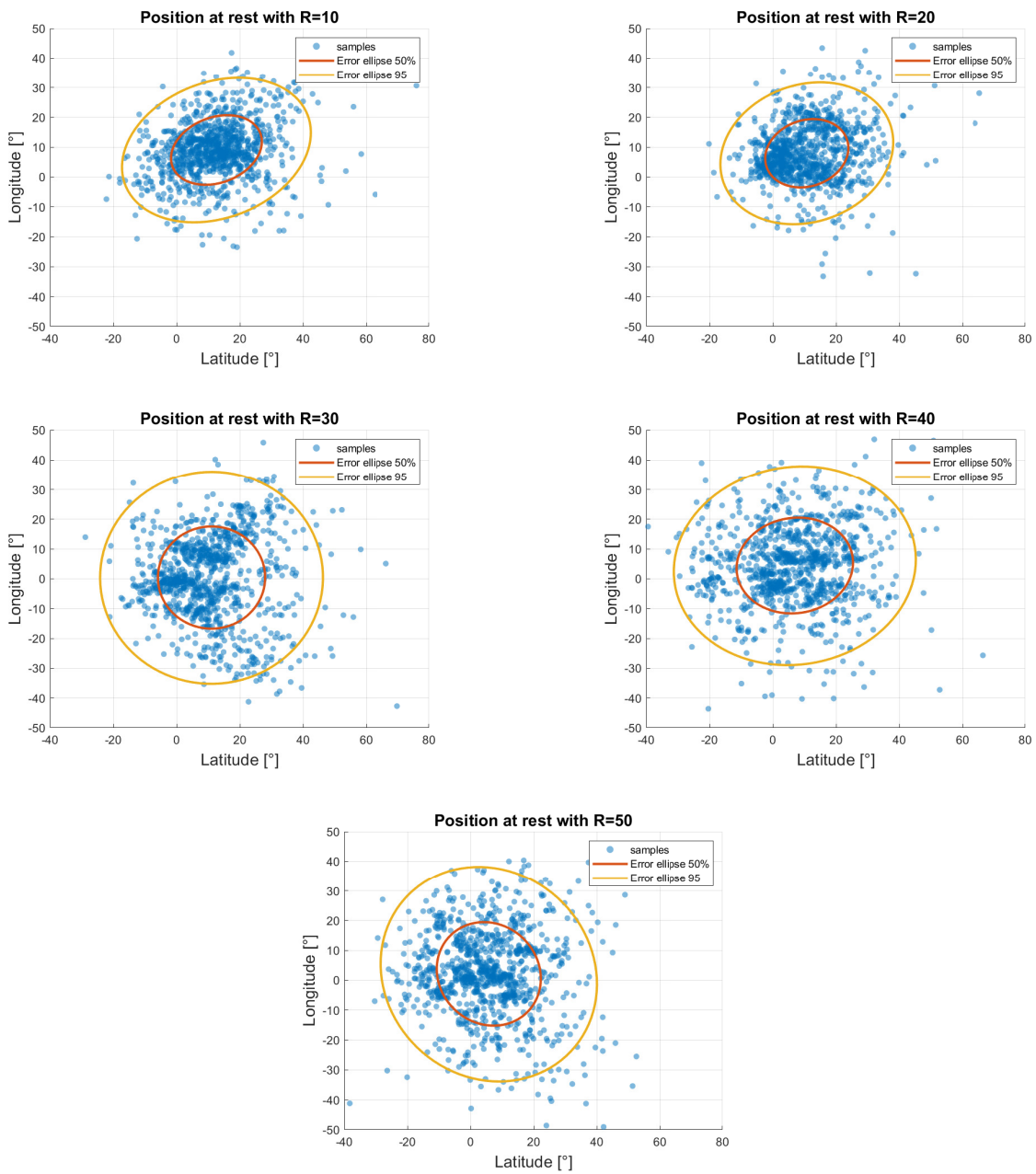
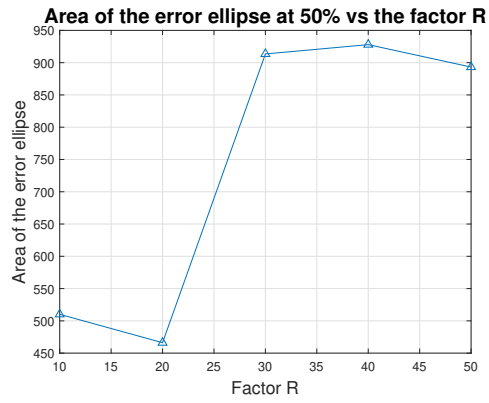
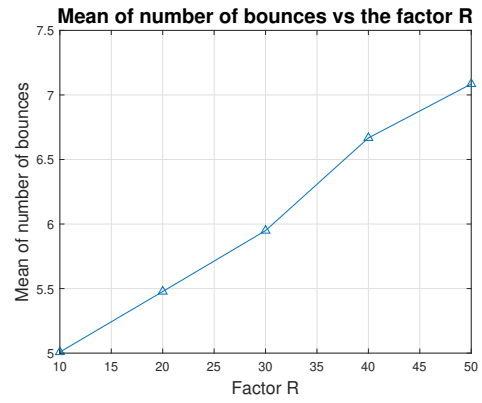


Figure 50: Position at rest with the ellipse error for different values for R.

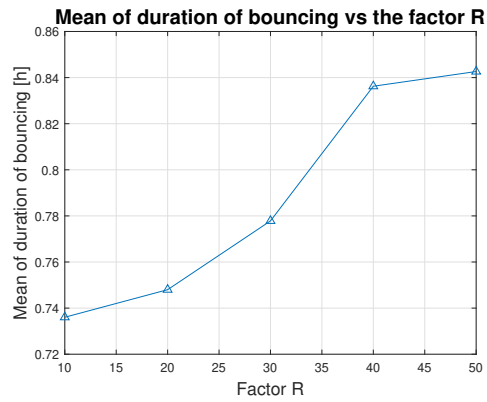




(a) Area of the error ellipse along the factor R.

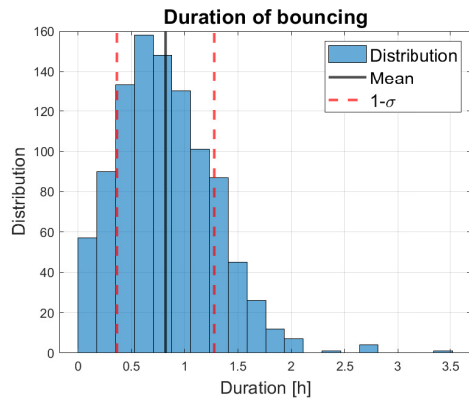


(b) Mean number of bounces along the factor R.

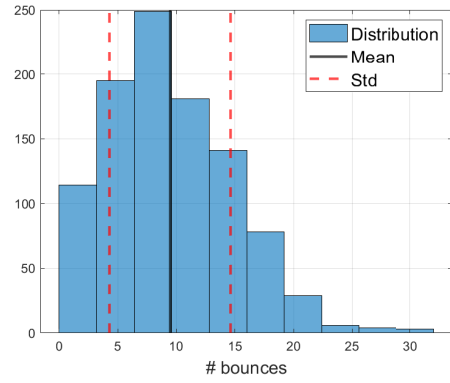


(c) Mean duration of bouncing along the factor R.

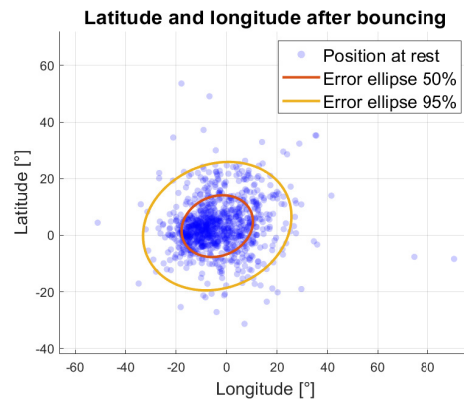
Figure 51: Different parameters for different shape models.



(a) Duration of bounces of the shape model with rocks.



(b) Number of bounces of the shape model with rocks.



(c) Position at rest of the shape model with rocks.

Figure 52: Distribution of different parameters for the shape model with rocks.

## 8 Conclusions

This work introduces a new model for the bounce motion. It accounts for the 3D shape of the satellite and its rotation. The consequences of it were studied on different surfaces. As such, the dependencies between different parameters have been shown.

In this chapter, first the improvements of the model will be explained from the first thesis to this work. Then, a talk about the implication of the mission is done in order to estimate the feasibility of the mission, followed by a small discussion on the impact of the terrain roughness. Finally, an insight on the future improvements that could be done on this work is made.

### 8.1 Improvements of the model

During this work, features were added or improved on the model. The main one is of course the integration of the 3D shape of Juventas, adding 3 degrees of liberty to the system. But other improves were made, like the detection of collision or the noise applied on the shape model. Everyone of them are summarized on the table 15.

Features	Vanhalst + Hanon [43]	Roisin [32]	This work
Propagator	Classic	Vectorized	Vectorized
Shape of Dimorphos	Ellipsoid	Ellipsoid + shape model	Shape model
Collision detection	Analytical (ellipsoid)	Distance to facets	Facet collision
Surface noise	Fractal Brownian	None	Perlin noise
Bouncing model	Coeff of rest.	Coeff of rest.	3D contact force
Juventas modeling	Point	Point	3D shape
Juventas' rotation	None	None	Computed inertia
Solar panels	None	None	Rigid panels with hinges

Table 15: Table of all improvements to the model, through the different thesis.

A great advantage of the code is its flexibility. The final algorithm is able to work different physic system, by changing the propagator. But it can also work on different shape models, an example is shown with a more complex asteroid on the figure 53.

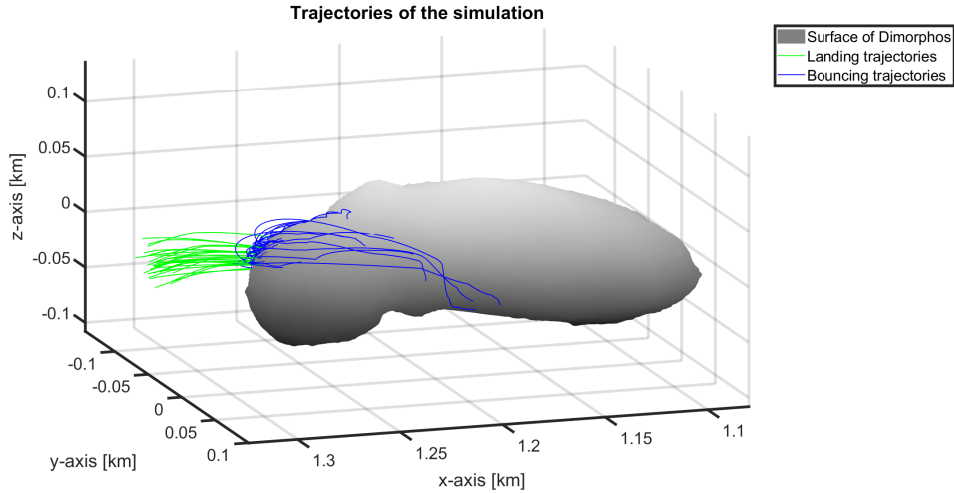


Figure 53: Trajectory of 30 samples on Itokawa.

## 8.2 Implication for the mission

Two main threats can compromise the mission.

First, if the bouncing on the surface is too strong, Juventas can bounce off and fail to land on Dimorphos. The simulations didn't show any case where it happens, leading to a rate of landing to 100%. We saw that including the 3D shape of Juventas and its rotation leads to bounces with smaller coefficient of restitution. This induces less risk of bounce off. Including the 3D shape of the spacecraft allows multiple micro-bounces and increases the energy damping. Furthermore, the solar panels can absorb a part of the kinetic energy as oscillations, which are slowly dissipated.

The second threat would be the bending of the solar panels. A too strong bending would curve the solar panels and make them nonoperational. Nonetheless, the maximum angle of deflection stayed well below the limit of  $90^\circ$ . We can conclude that the bending of the solar panels won't be a problem for the mission.

Those results are very optimistic regarding the mission. Still, the Monte-Carlo analysis has only been made on 1000 samples with no knowledge on the surface properties of Dimorphos.

## 8.3 Terrain roughness

The noise applied on the surface has a direct impact on different parameters of the bounce, especially on the dispersion after the bouncing. The roughness is then a very important characteristic that affects the dynamic of the bouncing of the CubeSat. Affecting also the duration of bouncing and the number of bounces.

## 8.4 Suggestions for Future Work

The work of this thesis could be improved by several ways :

- Use a shape model with non-uniform surface properties. Indeed, we could consider softer or harder surface on the asteroid to see new behaviors.
- Use a better propagator for the system. This work only accounts for a synchronous orbit of Dimorphos and no solar radiation pressure. A huge improvement would be to consider the new behavior of the system and adding orbital perturbations.
- Compare this model to experimental measurements. Testing the bouncing of rigid bodies at very low gravity is very challenging. Furthermore, the experiments would be able to fix the different constants to use.
- Considering the solar panels as flexible bodies. Instead of using 3 rigid bodies linked by torsion springs, the entire solar panel could be bent.
- A better modelization of the hinges. A simple model was used for the hinges, with no consideration for inelastic deformations. Include these deformations could be a huge improvement of the model.
- Decrease the RAM consumption. Indeed, the treatment in parallel use a lot of ram and do not allow to treat too many samples at the same time. Reducing the use of the RAM would unlock higher scale simulations.
- Accurate computation of the acceleration. The accelerometer inside Juventas should allow reconstructing the trajectory of the CubeSat. As such, emulate the measured acceleration are necessary to understand the motion of the bounce.
- Include the rotation of solar panels. The rotation of joints is unidimensional, nonetheless Juventas can rotate its solar panels in order to capture the sunlight more efficiently. Accounting for these rotations would add more realism to the model.

## Appendix

### Estimation of the coefficient of normal restitution

Considering a damped oscillator with the equation :

$$m\ddot{x} + \Gamma\dot{x} + kx = 0$$

Considering now  $\omega_0 = \sqrt{k/m}$  and  $\zeta = \Gamma/2\sqrt{km}$ , it becomes :

$$\ddot{x} + 2\zeta\omega_0\dot{x} + \omega_0^2x = 0$$

A solution for this differential equation is :

$$x(t) = e^{-t/\tau}(C \cos \omega_d t + D \sin \omega_d t)$$

with  $\omega_d = \omega_0\sqrt{1 - \zeta^2}$  and  $\tau = 2m/\Gamma$ .

We would like to compute, for an initial speed  $-v_0$ , how the speed will be restituted. Since  $x(0) = 0$ ,  $C = 0$  and since  $\dot{x} = -v_0$ ,  $D = -v_0/\omega_d$ . Now if we compute the acceleration, we have :

$$\begin{aligned}\ddot{x}(t) &= -\frac{1}{\tau^2}e^{-t/\tau}\frac{v_0}{\omega_d}\sin \omega_d t \\ &\quad + \frac{2}{\tau}e^{-t/\tau}v_0\cos \omega_d t \\ &\quad + e^{-t/\tau}v_0\omega_d\sin \omega_d t.\end{aligned}$$

Since the force is strictly positive,  $\ddot{x} > 0$ , let's find  $t'$  when  $\ddot{x} = 0$ , the equation becomes :

$$\begin{aligned}\left(\frac{1}{\tau^2}\frac{v_0}{\omega_d} - v_0\omega_d\right)\sin \omega_d t' &= \frac{2}{\tau}v_0\cos \omega_d t' \\ 2/\left(\frac{1}{\tau\omega_d} - \tau\omega_d\right) &= \tan \omega_d t' \\ t' &= \frac{\arctan\left(2/\left(\frac{1}{\tau\omega_d} - \tau\omega_d\right)\right)}{\omega_d} + \pi.\end{aligned}$$

Note that  $\pi$  is necessary on the last equation since we are looking for a solution in the second quadrant.

Knowing  $k$ ,  $m$  and  $\Gamma$ , we can then obtain  $\alpha$  as  $\dot{x}(t') = \alpha v_0$  :

$$\alpha = \frac{1}{\tau}e^{-t'/\tau}\frac{1}{\omega_d}\sin \omega_d t' - e^{-t'/\tau}\cos \omega_d t'$$

With this equation, we obtain for  $k = 10^6$  N/m,  $m = 12$  kg and  $\Gamma = 10^3$  N/m/s the value  $\alpha = 0.6597$ .

## Quaternion

The set of quaternion, noted  $\mathbb{H}$ , is a set of numbers that extends the real numbers. Similarly to complex numbers, they are composed of 3 imaginary number,  $i, j$  and  $k$  linked by the next relation :

$$i^2 = j^2 = k^2 = ijk = -1$$

As such, each quaternion can be written as composition of 4 real numbers:

$$q = a + bi + cj + dk$$

where  $a, b, c, d \in \mathbb{R}$ . The quaternion multiplication, noted  $*$ , is simply

$$\begin{aligned} q_1 * q_2 &= (a_1 + b_1i + c_1j + d_1k)(a_2 + b_2i + c_2j + d_2k) \\ &= a_1a_2 - b_1b_2 - c_1c_2 - d_1d_2 \\ &\quad + (a_1b_2 + b_1a_2 + c_1d_2 - d_1c_2)i \\ &\quad + (a_1c_2 + c_1a_2 + d_1b_2 - b_1d_2)j \\ &\quad + (a_1d_2 + d_1a_2 + b_1c_2 - c_1b_2)k \end{aligned}$$

The inverse of a quaternion is then

$$q^{-1} = \frac{1}{|q|^2}(a - bi - cj - dk)$$

where  $|q|^2 = qq^{-1} = a^2 + b^2 + c^2 + d^2$ . The true interest of using quaternion is how useful they are to describe rotations. Let's imagine a rotation of angle  $2\theta$  around an axis  $\mathbf{r} = (r_x, r_y, r_z)$  where  $|s| = 1$ . The quaternion associated to the rotation is defined as

$$q(\mathbf{r}, \theta) = \cos \theta + \sin \theta(r_x i + r_y j + r_z k)$$

Now, for a second rotation of angle  $\alpha$  around the axis  $2\mathbf{s} = (s_x, s_y, s_z)$  where  $|\mathbf{s}| = 1$ , the compisition of the 2 rotation is expressed as

$$q' = q(\mathbf{s}, \alpha) * q(\mathbf{r}, \theta) * q(\mathbf{s}, \alpha)^{-1}$$

This operation can be easily computed with a computer, and has the advantage to every information on the rotation in a single term. Usually, the quaternion defines the actual orientation of an object compared to a reference position. The rotation matrix is retrieved with the formula :

$$R(q) = \begin{pmatrix} a^2 + b^2 - c^2 - d^2 & 2bc - 2ad & 2ac + 2bd \\ 2ad + 2bc & a^2 - b^2 + c^2 - d^2 & 2cd - 2ab \\ 2bd - 2ac & 2ab + 2cd & a^2 - b^2 - c^2 + d^2 \end{pmatrix}$$

And for a angular velocity  $\boldsymbol{\omega} = (\omega_x, \omega_y, \omega_z)$ , the derivative of the orientation defined by  $q$  is

$$\dot{q} = \frac{q}{2} * (\omega_x i + \omega_y j + \omega_z k)$$

## Euler equation

Here is a demonstration of the Euler equation.

For a rigid body with an inertia tensor  $I \in \mathbb{R}^{3 \times 3}$ , its angular momentum in an inertial frame  $\mathcal{R}$  is given by

$$\mathbf{L} = I\boldsymbol{\omega}$$

where  $\boldsymbol{\omega}$  is the angular velocity.

The equation of motion is given by

$$\mathbf{M} = \frac{d\mathbf{L}}{dt} = \frac{d}{dt}(I\boldsymbol{\omega})$$

where  $\mathbf{M}$  is the angular momentum applied to the body.

The main issue of this equation is the presence of the inertia tensor, which is not independent of the time. To resolve this issue, let's introduce a frame  $\mathcal{R}'$  following the rigid body in its rotation, as such the body looks immobile in this frame. With a change of frame, and accounting for the virtual forces, the equation of motion becomes

$$\left( M = \frac{d\mathbf{L}}{dt} + \boldsymbol{\omega} \times \mathbf{L} = I\dot{\boldsymbol{\omega}} + \boldsymbol{\omega} \times \mathbf{L} \right)_{\mathcal{R}'}$$
$$\left( \dot{\boldsymbol{\omega}} = I^{-1}MI - I^{-1}(\boldsymbol{\omega} \times \mathbf{L}) \right)_{\mathcal{R}'}$$

Which gives the rotation of the rigid body along the time.



## References

1. *7017: TSR 0,5X3,5X3X12*. [N.d.]. Available also from: <https://catalog.lesjoforsab.com/product/7017-tsr-0-5x3-5x3x12>.
2. AL., Alan D. Berman et. Origin and Characterization of Different Stick-Slip Friction Mechanisms. *Langmuir*. 1996. Available from DOI: <https://doi.org/10.1021/la950896z>.
3. AL., Andrew F. Cheng et. Momentum transfer from the DART mission kinetic impact on asteroid Dimorphos. *Nature* 616, 457–460. 2023. Available from DOI: <https://doi.org/10.1038/s41586-023-05878-z>.
4. AL., Evgenij Zubko et. A family of embedded Runge-Kutta formulae. *Res. notes*. 2022. Available from DOI: [10.3847/2515-5172/ac9142](https://doi.org/10.3847/2515-5172/ac9142).
5. AL., HAJIME YANO et. Touchdown of the Hayabusa Spacecraft at the Muses Sea on Itokawa. *Science*. 2006. Available from DOI: <https://doi.org/10.1126/science.1126164>.
6. AL., Hajime Yano et. Touchdown of the Hayabusa Spacecraft at the Muses Sea on Itokawa. *SCIENCE*. 2006. Available from DOI: <https://doi.org/https://doi.org/10.1126/science.1126164>.
7. AL., Mehdi Scoubeau et. *JUVENTAS MECHANICAL ANALYSIS REPORT*. Gomspace Luxembourg, 2022.
8. AL., Patrick Michel et. European component of the AIDA mission to a binary asteroid: Characterization and interpretation of the impact of the DART mission. *Advances in Space Research*. 2018, vol. 62, no. 8, pp. 2261–2272. ISSN 0273-1177. Available from DOI: <https://doi.org/10.1016/j.asr.2017.12.020>. Past, Present and Future of Small Body Science and Exploration.
9. AL., Patrick Michel et. The ESA Hera Mission: Detailed Characterization of the DART Impact Outcome and of the Binary Asteroid (65803) Didymos. *Nature* 616, 457–460. 2022. Available from DOI: <https://doi.org/10.3847/PSJ/ac6f52>.
10. AL., Patrick Michel et. The ESA Hera mission to the binary asteroid (65803) Didymos: Planetary Defense and Science. *European Planetary Science Congress 2021*. 2021. Available from DOI: <https://doi.org/10.5194/epsc2021-71>.
11. AL., R. Terik Daly et. Successful kinetic impact into an asteroid for planetary defence. *Nature*. 2022. Available from DOI: <https://doi.org/10.1038/s41586-023-05810-5>.
12. AL., Thomas C.A. et. Orbital period change of Dimorphos due to the DART kinetic impact. *Nature*. 2023. Available from DOI: <https://doi.org/10.1038/s41586-023-05805-2>.
13. *DART's Final Images Prior to Impact*. [N.d.]. Available also from: <https://www.nasa.gov/feature/dart-s-final-images-prior-to-impact>.
14. *DART's Small Satellite Companion Tests Camera Prior to Dimorphos Impact*. [N.d.]. Available also from: <https://www.nasa.gov/feature/dart-s-small-satellite-companion-tests-camera-prior-to-dimorphos-impact>.

15. *Didymos: facts figures*. [N.d.]. Available also from: [https://www.esa.int/Space\\_Safety/Hera/Didymos\\_facts\\_figures](https://www.esa.int/Space_Safety/Hera/Didymos_facts_figures).
16. *Documentation about the sparial contact force used in Matlab Simscape multibody*. [N.d.]. Available also from: <https://nl.mathworks.com/help/sm/ref/spatialcontactforce.html>.
17. *Documentation about torsional spring in Matlab Simscape multibody*. [N.d.]. Available also from: <https://nl.mathworks.com/help/sm/ref/simscape.multibody.torsionalspringdamper-class.html>.
18. *Documentation of the noise generation of Blender*. [N.d.]. Available also from: [https://docs.blender.org/manual/en/latest/render/materials/legacy\\_textures/types/clouds.html](https://docs.blender.org/manual/en/latest/render/materials/legacy_textures/types/clouds.html).
19. DORMAND, J. R.; PRINCE, P. J. A family of embedded Runge-Kutta formulae. 1980.
20. DUIJSENS, Sébastien. *Master thesis : Cubesat deployment*. 2017.
21. *First Images from Italian Space Agency's LICIACube Satellite*. [N.d.]. Available also from: <https://www.nasa.gov/feature/first-images-from-italian-space-agency-s-liciacube-satellite>.
22. GASSOT, Oriane. *SAR imaging of an asteroid's regolith : simulation and data processing*. 2020. PhD thesis.
23. *Impactor Spacecraft. 2021 The Johns Hopkins University Applied Physics Laboratory*. [N.d.]. Available also from: <https://dart.jhuapl.edu/Mission/Impactor-Spacecraft.php>.
24. JAMES R. WERTZ David F. Everett, Jeffery J. Puschell. *Space Mission Engineering: The New SMAD*. Space Technology library, [n.d.].
25. M. POZZI, G. Maria Achili et al. Modeling and Simulation of Robotic Grasping in Simulink Through Simscape Multibody. *Front. Robot.* 2022. Available from DOI: <https://doi.org/10.3389/frobt.2022.873558>.
26. MCMAHON, Jay W. *An Analytical Theory for the Perturbative Effect of Solar Radiation Pressure on Natural and Artificial Satellites*. 2006. PhD thesis.
27. MIRTIC, Brian Vincent. *Impulse based Dynamic Simulation of Rigid Body System*. 1996. PhD thesis.
28. MUHAMMED, Lawal Nasir; UGHEOKE, Benjamin Iyenagbe; NWACHUKWU, Dorin Onyinye. Modeling and simulation of the kinematic behavior of the deployment mechanism of solar array for a 1-U CubeSat. *Engineering Reports*. [N.d.], vol. n/a, no. n/a, e12610. Available from DOI: <https://doi.org/10.1002/eng2.12610>.
29. NA, Jing; CHEN, Qiang; REN, Xuemei. Chapter 1 - Friction Dynamics and Modeling. In: NA, Jing; CHEN, Qiang; REN, Xuemei (eds.). *Adaptive Identification and Control of Uncertain Systems with Non-smooth Dynamics*. Academic Press, 2018, pp. 11–18. Emerging Methodologies and Applications in Modelling. ISBN 978-0-12-813683-6. Available from DOI: <https://doi.org/10.1016/B978-0-12-813683-6.00003-9>.

30. NAIDU, S.P.; BENNER, L.A.M.; BROZOVIC, M.; NOLAN, M.C.; OSTRO, S.J.; MARGOT, J.L.; GIORGINI, J.D.; HIRABAYASHI, T.; SCHEERES, D.J.; PRAVEC, P.; SCHEIRICH, P.; MAGRI, C.; JAO, J.S. Radar observations and a physical model of binary near-Earth asteroid 65803 Didymos, target of the DART mission. *Icarus*. 2020, vol. 348, p. 113777. ISSN 0019-1035. Available from DOI: <https://doi.org/10.1016/j.icarus.2020.113777>.
31. *Perlin Noise*. [N.d.]. Available also from: [https://en.wikipedia.org/wiki/Perlin\\_noise](https://en.wikipedia.org/wiki/Perlin_noise).
32. ROISIN, Guillaume. *Landing trajectories analysis and geophysics of Juventas in the binary asteroid system Didymos*. 2022. PhD thesis.
33. ROMANO, Rodrigo A.; GARCIA, Claudio. KARNOPP FRICTION MODEL IDENTIFICATION FOR A REAL CONTROL VALVE. *IFAC Proceedings Volumes*. 2008, vol. 41, no. 2, pp. 14906–14911. ISSN 1474-6670. Available from DOI: <https://doi.org/10.3182/20080706-5-KR-1001.02523>. 17th IFAC World Congress.
34. SCHAUB, Hanspeter; JUNKINS, John L. *ANALYTICAL MECHANICS of AEROSPACE SYSTEMS*. 2002.
35. SCOUBEAU, Mehdi; TEAM, GMV. Juventas Mission Analysis Report (MAR). *JUVGS-MAR-001*. 2022.
36. *Simscape multibody documentation*. [N.d.]. Available also from: <https://nl.mathworks.com/help/sm/>.
37. *Technology demonstration*. [N.d.]. Available also from: [https://www.esa.int/Space\\_Safety/Hera/Technology\\_demonstration2](https://www.esa.int/Space_Safety/Hera/Technology_demonstration2).
38. *Theorema egregium*. [N.d.]. Available also from: [https://fr.wikipedia.org/wiki/Theorema\\_egregium](https://fr.wikipedia.org/wiki/Theorema_egregium).
39. *Torsion Springs - Part number Febrotec: 0T020-270-093*. [N.d.]. Available also from: <https://www.febrotec.de/en/torsion-springs/0t020-270-093/?lang=en&country=&set=TRUE>.
40. V., Szebehely. *theory of orbit: the restricted problem of three bodies*. 2012.
41. VAN WAL, Stefaan; ÇELIK, Onur; TSUDA, Yuichi; YOSHIKAWA, Kent; KAWAKATSU, Yasuhiro. Reduced-gravity experiments of nonspherical rigid-body impact on hard surfaces. *Advances in Space Research*. 2021, vol. 67, no. 1, pp. 436–476. ISSN 0273-1177. Available from DOI: <https://doi.org/10.1016/j.asr.2020.10.018>.
42. VAN WAL, Stefaan; REID, Robert G.; SCHEERES, Daniel J. Simulation of Nonspherical Asteroid Landers: Contact Modeling and Shape Effects on Bouncing. *Journal of Spacecraft and Rockets*. 2020, vol. 57, no. 1, pp. 109–130. Available from DOI: [10.2514/1.A34573](https://doi.org/10.2514/1.A34573).
43. VANHALST, Guillaume; HANON, Guillaume. *A study of the landing phase of the Juventas CubeSat on the moon of the binary asteroid system Didymos*. 2020. PhD thesis.

44. WOJTYRA, Marek. Modeling of static friction in closed-loop kinematic chains—Uniqueness and parametric sensitivity problems. 2016. Available from DOI: DOI10.1007/s11044-016-9535-6.
45. ZHANG, Jing; YAN, Kai; KOU, Ziming. Design and Analysis of Flexible Hinge Used for Unfolding Spacecraft Solar Panels. *Journal of Aerospace Technology and Management*. 2019, vol. 11, e3319. ISSN 2175-9146. Available from DOI: 10.5028/jatm.v11.1060.